

Hydrodynamic and thermodynamic non-equilibrium characteristics of shock waves: Insights from the discrete Boltzmann method

Dejia Zhang^{a,b}, Yanbiao Gan^{c,*}, Bin Yang^d, Yiming Shan^e, Aiguo Xu^{b,f,g,h,*}

^aSchool of Physical Science and Technology, Guangxi University, Nanning 530004, China

^bNational Key Laboratory of Computational Physics, Institute of Applied Physics and Computational Mathematics, Beijing 100088, China

^cHebei Key Laboratory of Trans-Media Aerial Underwater Vehicle, North China Institute of Aerospace Engineering, Langfang 065000, China

^dSchool of Energy and Safety Engineering, Tianjin Chengjian University, Tianjin 300384, China

^eCollege of Forensic Science, Criminal Investigation Police University of China, Shenyang 110854, China

^fState Key Laboratory of Explosion Science and Safety Protection, Beijing Institute of Technology, Beijing 100081, China

^gNational Key Laboratory of Shock Wave and Detonation Physics, Mianyang 621999, China

^hHEDPS, Center for Applied Physics and Technology, and College of Engineering, Peking University, Beijing 100871, China

arXiv:2502.06326v1 [physics.flu-dyn] 10 Feb 2025

Abstract

Shock waves are typical non-equilibrium phenomena in nature and engineering, driven by hydrodynamic non-equilibrium (HNE) and thermodynamic non-equilibrium (TNE) effects. However, the mechanisms underlying these non-equilibrium effects are not fully understood. In this study, we develop the discrete Boltzmann method (DBM) by directly discretizing velocity space, allowing for the adequate capture of higher-order HNE and TNE effects. To reveal these mechanisms, we derive analytical solutions for distribution functions and TNE quantities at various orders using Chapman-Enskog analysis, although DBM simulations do not rely on these theoretical derivations. Using argon shock structures as a case study, DBM simulations of interface profiles and thickness at the macroscopic level agree well with experimental data and direct simulation Monte Carlo results. At the mesoscopic level, DBM-derived distribution functions and TNE measures closely match their corresponding analytical solutions. The effect of Mach number on HNE is analyzed by examining the shape and thickness of density, temperature, and velocity interfaces. Key findings include: (i) Mach number induces a two-stage effect on macroscopic quantities, influencing both interface smoothness and thickness, and (ii) as Mach number increases, the region of strong compressibility shifts from the outflow region to the inflow region. As for TNE characteristics, increasing Mach number significantly amplifies TNE intensity and expands the non-equilibrium region. Distribution functions at different shock locations exhibit variations in amplitude, shape, and deviation from equilibrium, are analyzed theoretically. These findings highlight the close connection between macroscopic and mesoscopic non-equilibrium behaviors and emphasize that non-equilibrium manifestations depend on the analytical perspective. This research provides kinetic insights into the multiscale nature and effects of non-equilibrium characteristics in shock waves, offering theoretical references for constructing kinetic models that describe different types and orders of non-equilibrium effects.

Keywords: shock wave, thermodynamic non-equilibrium, hydrodynamic non-equilibrium, discrete Boltzmann method

1. Introduction

Shock waves, a hallmark of supersonic flow, are prevalent in both natural phenomena and engineering applications. Examples include collisionless shocks during supernova remnant evolution [1], laser-induced shocks in inertial confinement fusion (ICF) [2], shocks encountered in supersonic and hypersonic vehicles [3], and those generated by medical devices for kidney stone treatment [4]. With the rapid advancements in aerospace and energy-related fields, shock wave research has gained increasing attention. For example, shock

wave/boundary layer interactions in scramjet engines are extensively studied due to their critical role in enhancing intake and combustion efficiency [5–7]. Shock wave propagation and evolution significantly affect fluid system performance. In supersonic combustion systems, shock waves deform fuel droplets, thereby affecting fuel mixing, combustion efficiency, and overall performance metrics [8, 9]. In shock tubes, interactions between shock waves and walls or mechanical interfaces generate complex wave structures, which in turn shape intricate flow dynamics [10–12]. Moreover, the growing importance of small-scale structures and rapid dynamics in engineering highlights the need to investigate the internal structure of shock waves.. Cai *et al.* demonstrated that in indirectly driven laser ICF, increased ion-ion mean free paths during gold-wall and target plasma interactions lead to collisionless shock waves, significantly affecting implosion neutron yield [13].

Shock wave flow, as a typical form of non-equilibrium flow, driven by small-scale structures and rapid dynamic modes, has

*Corresponding author at: Hebei Key Laboratory of Trans-Media Aerial Underwater Vehicle, North China Institute of Aerospace Engineering, Langfang 065000, China

**Corresponding author at: National Key Laboratory of Computational Physics, Institute of Applied Physics and Computational Mathematics, P. O. Box 8009-26, Beijing 100088, China

Email addresses: Gan@nciae.edu.cn (Yanbiao Gan), Xu_Aiguo@iapcm.ac.cn (Aiguo Xu)

been extensively studied in recent years due to its importance in various scientific and engineering contexts [14–23]. The shock wave thickness is several times larger than the mean molecular free path, leading to a highly discrete internal structure that deviates significantly from thermodynamic equilibrium. Mott-Smith first identified that the strong non-equilibrium nature of shock waves results in bimodal molecular velocity distributions within the shock region [24]. Under these conditions, he derived an analytical solution for the spatial structure of strong shock waves by solving the transport equation. Bird later developed the direct simulation Monte Carlo (DSMC) method to solve the Boltzmann equation using a Monte Carlo algorithm [25]. The DSMC method has been extensively validated for various non-equilibrium flows, including shock wave structures. Alsmeyer measured the density profiles of argon and nitrogen shock waves with Mach numbers ranging from 1.5 to 10.0 using electron beam experiments [26]. His study compared the results with Bird’s Monte Carlo simulations, Mott-Smith’s theory, the Navier-Stokes (NS) equations, and the Burnett equations. Pham-Van-Diep *et al.* measured the velocity distribution function in a Mach 25 helium shock wave [27]. Their experimental results were the first to confirm the bimodal nature of the velocity distribution predicted by Mott-Smith’s theory.

Initially, the NS equations, based on continuity assumptions and near-equilibrium approximations, were employed to model shock structures [28]. However, the NS equations neglect second-order and higher-order nonequilibrium effects, limiting their applicability to Mach numbers below approximately 1.3 [26]. To extend the applicability of continuum models, Foch applied the Burnett equations to model shock structures at Mach numbers up to 1.9 [29]. The Burnett equations, derived from Chapman-Enskog (CE) theory, incorporate second-order Knudsen (Kn) number effects, offering improved accuracy over the NS equations [29, 30]. Beyond continuum-based approaches, kinetic methods based on the Boltzmann equation have emerged as powerful tools for studying shock structures. These methods include the direct simulation Monte Carlo (DSMC) method, improved Burnett and super-Burnett equations from kinetic theory [31], Grad’s moment method [32], regularized 13-moment equations [33, 34], and the lattice Boltzmann method [35–42]. Recent advances in kinetic methods include the unified gas-kinetic scheme (UGKS) [43–45], discrete unified gas-kinetic scheme (DUGKS) [46], unified gas-kinetic wave-particle methods [47–49], and kinetic models for monatomic gas mixtures [50]. Additionally, nonlinear coupled constitutive relations [15, 51], gas-kinetic unified algorithms [52, 53], and particle-on-demand-based kinetic schemes [54, 55] have further advanced shock structure modeling. Other effective methods include the discrete velocity method [56] and the discrete Boltzmann method [57], both of which provide valuable insights into the intricate dynamics of shock structures under various flow regimes.

Shock waves are widely used as benchmarks to validate algorithm accuracy in current studies. However, the non-equilibrium characteristics and underlying mechanisms of shock waves, which critically influence fluid system perfor-

mance, remain poorly understood. Within the framework of DBM, non-equilibrium effects can be classified into two categories: hydrodynamic non-equilibrium (HNE) and thermodynamic non-equilibrium (TNE) [57]. HNE describes non-equilibrium through spatial variations in macroscopic quantities (e.g., density, temperature, velocity, and pressure), while TNE reflects mesoscopic kinetic characteristics, such as distribution functions and TNE-specific quantities. TNE provides the physical foundation for understanding HNE.

The discrete Boltzmann model (DBM) is a kinetic approach for modeling discrete/non-equilibrium flows and analyzing complex physical fields [57, 58]. From a physical modeling perspective, DBM is a direct kinetic approach that eliminates the need to derive and solve complex hydrodynamic equations, such as those in the Burnett and Grad moment methods. The physical function of DBM is equivalent to the evolution equations, incorporating not only conserved moments but also some closely related non-conserved moments. The DBM simulation does not rely on the CE multiscale analysis. In DBM, CE analysis serves two purposes: (i) identifying non-conserved kinetic moments relevant to system states and features, and (ii) offering an intuitive understanding of discrete/non-equilibrium mechanisms. For complex physical field analysis, DBM provides a set of analytical schemes capable of checking, describing, manifesting and analyzing the discrete/nonequilibrium states and effects, which are difficult to capture using NS model and other kinetic methods. DBM has been extensively applied to non-equilibrium phenomena, including multiphase flows [59, 60], hydrodynamic instabilities [61–65], microscale flows [66], combustion and detonation dynamics [67], and plasma systems [68]. Numerous studies have highlighted the critical role of thermodynamic non-equilibrium (TNE) behavior in determining system performance [61–63, 66]. Notable examples include: Chen *et al.* examined how the shock Mach number influences the interplay between Rayleigh-Taylor and Richtmyer-Meshkov (RM) instabilities, analyzing its correlation with TNE and HNE behaviors [69]. Song *et al.* proposed that non-equilibrium characteristic quantities serve as physical criteria for assessing whether a magnetic field can prevent interface inversion in plasma RM instability systems [68]. Zhang *et al.* investigated how shock waves influence entropy production during shock-bubble interactions [70]. Gan *et al.* investigated HNE-TNE interactions in phase separation and demonstrated that TNE intensity provides a robust criterion for distinguishing spinodal decomposition from domain growth [59, 60].

To further extract, illustrate and study the HNE and TNE effects overlooked by other simulation methods, we develop a DBM model that incorporates sufficiently higher-order Knudsen number effect, and investigate the HNE and TNE behaviors inside argon normal shock structures with Mach numbers ranging from 1.2 to 12.0. The remainder of this paper is organized as follows. The remainder of this paper is organized as follows. Section 2 outlines the DBM modeling framework and the analysis scheme for TNE characteristics. Section 3 presents the derivation of TNE quantities. Section 4 details the simulation setup and presents the numerical results of the internal shock

structure. Finally, Section 5 summarizes the key findings of this study.

2. DBM modeling and complex physical field analysis method

2.1. DBM equation for normal shock wave

For a normal shock wave propagating along the x -axis, the simplified Boltzmann equation with the Shakhov collision model is employed:

$$\frac{\partial f}{\partial t} + v_x \cdot \frac{\partial f}{\partial x} = -\frac{1}{\tau}(f - f^s), \quad (1)$$

with the Shakhov distribution function

$$f^s = f^{eq} + f^{eq} \cdot \left[(1 - \text{Pr}) \cdot c_x q_x \cdot \frac{c_x^2 + \eta^2}{(n+3)pRT} \right]. \quad (2)$$

and the equilibrium distribution function

$$f^{eq} = \rho \left(\frac{1}{2\pi RT} \right)^{(1+n)/2} \exp \left(-\frac{c_x^2 + \eta^2}{2RT} \right). \quad (3)$$

Here, f represents the distribution function, and r_α and v_α denote the fluid's spatial position and particle velocity in the α -direction, respectively. The parameter τ represents the relaxation time of molecular collisions, defined as the reciprocal of the collision frequency. The variables ρ , u_x , T , and p denote the fluid's mass density, velocity, temperature, and pressure, respectively. The ideal gas equation of state, $p = \rho RT$, is used to simulate the argon shock wave, where R is the gas constant. q_x represents the heat flux. The parameter η accounts for additional degrees of freedom beyond translational motion, described by n . For instance, when $n = 2$, $\eta^2 = \eta_1^2 + \eta_2^2$. When the Prandtl number is $\text{Pr} = 1$, the collision operator in Eq. (1) is simplified to the BGK operator. In fact, the BGK operator used in the research field of non-equilibrium flow is modified by the mean field theory [57, 60].

Despite spatial simplification, the distribution function f remains high-dimensional, expressed as $f = f(x, v_x, \eta)$. To address this, we introduce two reduced distribution functions. Specifically, the evolution of Eq. (1) can be transformed into the evolution of two reduced distribution functions, as:

$$\frac{\partial}{\partial t} \begin{Bmatrix} g \\ h \end{Bmatrix} + v_x \cdot \frac{\partial}{\partial x} \begin{Bmatrix} g \\ h \end{Bmatrix} = -\frac{1}{\tau} \begin{Bmatrix} g - g^s \\ h - h^s \end{Bmatrix}. \quad (4)$$

The two reduced distribution functions are defined as:

$$g = \int f d\eta, \quad (5)$$

and

$$h = \int f \frac{\eta^2}{2} d\eta. \quad (6)$$

Physically, the reduced distribution function g describes the evolution of density and velocity, while h captures the influence of additional degrees of freedom on temperature. When $f = f^{eq}$, we get

$$g^{eq} = \int f^{eq} d\eta = \rho \left(\frac{1}{2\pi RT} \right)^{1/2} \exp \left(-\frac{c_x^2}{2RT} \right), \quad (7)$$

and

$$h^{eq} = \int f^{eq} \frac{\eta^2}{2} d\eta = \frac{nRT}{2} g^{eq}. \quad (8)$$

The expressions of g^s and h^s in Eq. (4) are

$$g^s = g^{eq} + g^{eq} \left[(1 - \text{Pr}) \cdot c_x q_x \cdot \frac{\frac{c_x^2}{RT} - 3}{(n+3)pRT} \right], \quad (9)$$

and

$$h^s = h^{eq} + h^{eq} \left[(1 - \text{Pr}) \cdot c_x q_x \cdot \frac{\frac{c_x^2}{RT} - 1}{(n+3)pRT} \right]. \quad (10)$$

Macroscopic quantities are obtained by evaluating three conserved kinetic moments of the distribution function,

$$\rho = \int g dv_x, \quad (11)$$

$$\rho u_x = \int g v_x dv_x, \quad (12)$$

and

$$\frac{1+n}{2} \rho RT = \int (g \frac{c_x^2}{2} + h) dv_x. \quad (13)$$

The viscous stress and heat flux are given by

$$\Pi = \int (g - g^{eq}) c_x c_x dv_x, \quad (14)$$

and

$$q = \int \left[(g - g^{eq}) \frac{c_x^2}{2} + (h - h^{eq}) \right] c_x dv_x. \quad (15)$$

2.2. DBM with higher-order TNE effects

In this section, we aim to maximize the DBM model's capability in capturing non-equilibrium effects. To achieve this, two strategies exist: one based on Chapman-Enskog (CE) analysis and the other independent of it [57].

The first strategy enhances DBM's capability to capture non-equilibrium effects, starting from the equilibrium state. Kinetic theory characterizes a system through the distribution function f and its kinetic moments. Consequently, DBM preserves the kinetic moments governing physical behavior before and after velocity space discretization:

$$\int f \Psi(v, \eta) dv d\eta = \sum f_i \Psi(v_i, \eta_i). \quad (16)$$

CE analysis provides an efficient approach for identifying the kinetic moments essential for capturing non-equilibrium effects. Retaining additional kinetic moments improves DBM's

ability to capture non-equilibrium effects and extends its applicability to higher Knudsen numbers [60, 71].

Specifically, for continuum flows ($\text{Kn} < 0.001$), seven kinetic moments ($M_0, M_1, M_{2,0}, M_2, M_{3,1}, M_3$, and $M_{4,2}$) must be retained before and after discretization. In the transition regime ($0.1 < \text{Kn} < 10$), second- and higher-order TNE effects become significant and must be considered. To capture second-order TNE effects, two additional kinetic moments, M_4 and $M_{5,3}$, need to be retained. For third-order TNE effects, two additional kinetic moments, M_5 and $M_{6,4}$, should also be included. Further details on DBM modeling using CE analysis are provided in Section 3. As discretization levels and non-equilibrium effects increase, DBM's complexity grows more slowly than that of kinetic macroscopic modeling (e.g., deriving and solving extended hydrodynamic equations), as it requires only a limited number of additional kinetic moments. Therefore, this method is both straightforward and computationally efficient. Notably, this method retains a limited set of kinetic moments. While these moments have clear physical meanings, f_i itself lacks direct physical interpretation.

An alternative approach to describing non-equilibrium flows in DBM involves directly discretizing the particle velocity space with a sufficiently large number of grid points, rather than relying on a fixed discrete velocity stencil. This method maximizes the retention of non-conserved kinetic moments, enhancing the accuracy of non-equilibrium effect characterization. Building on this foundation, Zhang *et al.* developed a steady-state DBM tailored for non-equilibrium flows at the micro-nanoscale [70]. The model effectively captures gas flow behaviors across a broad range of rarefaction parameters, spanning from slip flow to free molecular flow. Since this approach retains a potentially infinite number of kinetic moments, the discrete particle velocity v_i closely approximates the true particle velocity v , and the discrete distribution function f_i accurately represents the continuous distribution function f . *Consequently, not only do the kinetic moments of f_i retain clear physical meanings, but f_i itself also carries a direct physical interpretation.*

In the steady-state DBM, the time derivative of f is set to zero, which allows for a more in-depth exploration of non-equilibrium effects at the expense of the model's applicability over extended time spans. In contrast, the time-dependent DBM reduces the system's descriptive capability from potentially infinite kinetic moments of f to a finite set of moments. Thus, the time-dependent and steady-state DBMs are complementary. Based on these approaches, this paper extends the steady-state DBM to an unsteady-state version that captures non-equilibrium flows across the entire time domain. The extended model achieves high accuracy in describing TNE effects and enables the study of the system's kinetic characteristics.

2.3. Scheme for extracting and analyzing TNE characteristics

The Kn number is commonly used to characterize the degree of non-equilibrium in complex flows. However, the Kn number, whether local or global, is a coarse-grained quantity that cannot fully capture all non-equilibrium characteristics of a flow system. Recent studies show that relying solely on the Kn number

gives an incomplete and potentially misleading view of non-equilibrium phenomena [57, 60, 71, 72]. Therefore, in addition to traditional physical quantities used in fluid modeling, such as the Kn number, macroscopic gradients, relaxation time τ , and the distribution function, introducing additional TNE characteristic quantities is crucial. These quantities provide a more detailed and comprehensive understanding of the complex features of non-equilibrium systems.

In the framework of DBM, the non-conserved kinetic moments of $(f - f^{eq})$ can be utilized to describe both the state of a system deviating from continuum/equilibrium and the effects resulting from this deviation [73]. To illustrate this, we take the TNE quantities in the x direction as an example:

$$\Delta_m^* = \int (g - g^{eq}) c_x^m dv_x, \quad (17)$$

and

$$\Delta_{m,n}^* = \int \left[(g - g^{eq}) \frac{c_x^{m-n}}{2} + (h - h^{eq}) \right] c_x^n dv_x, \quad (18)$$

where m indicates the total power of c_x and n denotes the contraction of the m -th tensor into an n -th order tensor. When $m = 2$, the TNE quantity Δ_2^* , representing the flux of momentum (known as the non-organized momentum flux, NOMF), is given by

$$\Delta_2^* = \int (g - g^{eq}) c_x^2 dv_x. \quad (19)$$

In addition to characterizing momentum flux, Δ_2^* also represents the internal energy associated with the x -direction degree of freedom. For $m = 3$ and $n = 1$, the TNE quantity $\Delta_{3,1}^*$, describing the flux of total energy (known as non-organized energy flux, NOEF) is expressed as

$$\Delta_{3,1}^* = \int \left[(g - g^{eq}) \frac{c_x^2}{2} + (h - h^{eq}) \right] c_x dv_x. \quad (20)$$

The TNE quantity Δ_2^* corresponds to the generalized viscous stress Π in hydrodynamic descriptions, and $\Delta_{3,1}^*$ corresponds to the generalized heat flux q . TNE analysis provides insights into the mechanisms underlying HNE descriptions. To explore TNE behaviors further, higher-order TNE quantities, including Δ_3^* , Δ_4^* , Δ_5^* , $\Delta_{4,2}^*$, $\Delta_{5,3}^*$, and $\Delta_{6,4}^*$, are defined. Each TNE quantity characterizes the system's non-equilibrium properties from a unique perspective. A natural step is to define a generalized TNE vector, $S_{TNE} = \{\Delta_2^*, \Delta_{3,1}^*, \Delta_3^*, \Delta_{4,2}^*, \Delta_4^*, \Delta_{5,3}^*, \dots\}$, providing a multi-perspective, cross-dimensional description of non-equilibrium states and behaviors.

The definitions in Eqs. (17) and (18) represent the total summation of all orders of TNE, as $g - g^{eq} = g^{(1)} + g^{(2)} + g^{(3)} + \dots$. When the fluid is in equilibrium, $g \approx g^{eq}$, and the TNE in Eqs. (17) and (18) are zero. For the first-order TNE (the first-order Kn number), $g - g^{eq} \approx g^{(1)}$. The first-order TNE quantities, $\Delta_m^{*(1)}$ and $\Delta_{m,n}^{*(1)}$, are obtained. In this case, Δ_m^* and $\Delta_{m,n}^*$ are TNE quantities up to the first-order TNE. When $g - g^{eq} \approx g^{(1)} + g^{(2)}$, we have $\Delta_m^* = \Delta_m^{*(1)} + \Delta_m^{*(2)}$ and $\Delta_{m,n}^* = \Delta_{m,n}^{*(1)} + \Delta_{m,n}^{*(2)}$, where $\Delta_m^{*(2)}$ and $\Delta_{m,n}^{*(2)}$ are second-order TNE quantities, and Δ_m^* and $\Delta_{m,n}^*$ are TNE quantities up to the second-order TNE. Similarly,

Perspectives	Physical meanings
k th-order Kn number effects	Retention of terms up to the k th-order of the Knudsen number in CE analysis.
$g - g^{eq}$	Deviation of the DF g from the equilibrium DF g^{eq} .
$g^{(k)}$	k th-order deviation of the DF g from the equilibrium DF g^{eq} .
$\Delta_m^*, \Delta_{m,n}^*$	Non-conserved central kinetic moments of $(g - g^{eq})$, representing the total summation of all orders of TNE effects.
Δ_2^*	Non-organized momentum flux (NOMF), or the internal energy in the x degree of freedom.
$\Delta_{3,1}^*$	Non-organized energy flux (NOEF), or heat conduction in the x direction.
$\Delta_m^{*(k)}, \Delta_{m,n}^{*(k)}$	Non-conserved central kinetic moments of $(g - g^{eq})$, representing the k -order TNE effects.
$\Delta_m, \Delta_{m,n}$	Non-conserved kinetic moments of $g - g^{eq}$, representing the total summation of all orders of HNE+TNE effects.
$\Delta_m^{(k)}, \Delta_{m,n}^{(k)}$	Non-conserved kinetic moments of $(g - g^{eq})$, representing the k -order HNE+TNE effects.
$\mathcal{S}_{\text{TNE}} = \{\text{Kn}, g - g^{eq}, g^{(k)}, \Delta_2^*, \Delta_{3,1}^*, \Delta_3^*, \Delta_{4,2}^*, \Delta_4^*, \Delta_{5,3}^*, \Delta_5^*, \Delta_{6,4}^*\}$	Multi-perspective, cross-dimensional description of non-equilibrium states and behaviors.

Table 1: Perspectives used to characterize the non-equilibrium states and behaviors in this paper, where DF denotes the distribution function.

$\Delta_m^{*(3)}$ and $\Delta_{m,n}^{*(3)}$ are third-order TNE quantities. For clarity, we list in Table 1.

3. CE multi-scale analysis and derivation of TNE measures

This section performs CE multi-scale analysis to reveal the driving mechanisms of non-equilibrium flows and derives analytical expressions for TNE quantities. In fact, DBM modeling does not rely on CE analysis, and numerical simulations can be conducted independently.

3.1. Hydrodynamic equations

We begin with the Shakhov-Boltzmann equation (1). In CE analysis, the distribution functions are expanded around the equilibrium distribution function

$$f = f^{eq} + \text{Kn} f^{(1)} + \text{Kn}^2 f^{(2)} + \dots, \quad (21)$$

and

$$f^s = f^{eq} + \text{Kn} f^{s(1)} + \text{Kn}^2 f^{s(2)} + \dots. \quad (22)$$

The temporal and spatial derivatives are also expanded as

$$\frac{\partial}{\partial t} = \text{Kn} \frac{\partial}{\partial t_1} + \text{Kn}^2 \frac{\partial}{\partial t_2} + \dots, \quad (23)$$

and

$$\frac{\partial}{\partial x} = \text{Kn} \frac{\partial}{\partial x_1} + \dots. \quad (24)$$

Substituting the expanded distribution functions and derivatives into Eq. (1), we obtain:

$$\begin{aligned} & (\text{Kn} \frac{\partial}{\partial t_1} + \text{Kn}^2 \frac{\partial}{\partial t_2} + \dots)(f^{eq} + \text{Kn} f^{(1)} + \text{Kn}^2 f^{(2)} + \dots) \\ & v_x \text{Kn} \frac{\partial}{\partial x_1} (f^{eq} + \text{Kn} f^{(1)} + \text{Kn}^2 f^{(2)} + \dots) \\ & = -\frac{1}{\tau} [(f^{eq} + \text{Kn} f^{(1)} + \text{Kn}^2 f^{(2)} + \dots) \\ & - (f^{eq} + \text{Kn} f^{s(1)} + \text{Kn}^2 f^{s(2)} + \dots)] \end{aligned} \quad (25)$$

Extracting the first-order terms of the Kn number yields

$$\frac{\partial f^{eq}}{\partial t_1} + v_x \frac{\partial f^{eq}}{\partial x} = -\frac{1}{\tau} (f^{(1)} - f^{s(1)}). \quad (26)$$

In the following and here x_1 is replaced by x . By applying the first three orders of conserved kinetic moment operators, namely, $\int dv_x d\eta$, $\int v_x dv_x d\eta$, and $\int \frac{1}{2}(v_x^2 + \eta^2) dv_x d\eta$ into Eq. (26), we can derive the Euler equations:

$$\frac{\partial \rho}{\partial t_1} + \frac{\partial(\rho u_x)}{\partial x} = 0, \quad (27)$$

TNE quantities	Physical meanings	Analytical expressions
Δ_2^*	NOMF	$\Delta_2^{*(1)} = -\frac{4}{3}\tau\rho T \frac{\partial u_x}{\partial x}$ $\Delta_2^{*(2)} = -\frac{4}{3\text{Pr}}\tau^2 \left\{ (\text{Pr}-1)\rho T \frac{\partial^2 T}{\partial x^2} + \text{Pr}T^2 \frac{\partial^2 \rho}{\partial x^2} - \text{Pr} \frac{T^2}{\rho} \left(\frac{\partial \rho}{\partial x} \right)^2 \right. \\ \left. + (\text{Pr}-1)T \frac{\partial T}{\partial x} \frac{\partial \rho}{\partial x} + \rho \left[\frac{\text{Pr}T}{3} \left(\frac{\partial u_x}{\partial x} \right)^2 - \left(\frac{\partial T}{\partial x} \right)^2 \right] \right\}$
$\Delta_{3,1}^*$	NOEF	$\Delta_{3,1}^{*(1)} = -\frac{5}{2\text{Pr}}\tau\rho T \frac{\partial T}{\partial x}$ $\Delta_{3,1}^{*(2)} = \frac{14\tau^2}{3\text{Pr}^2} \left[\frac{2}{7}(\text{Pr}-\frac{5}{4})T \frac{\partial^2 u_x}{\partial x^2} + (\text{Pr}-\frac{1}{14}) \frac{\partial u_x}{\partial x} \frac{\partial T}{\partial x} \right]$ $\Delta_{3,1}^{*(3)} = -\frac{77}{3\text{Pr}^3}\tau^3 \frac{1}{\rho^2} \left\{ -\frac{4}{77}(\text{Pr}^2-7\text{Pr}+\frac{25}{8})\rho^3 T^2 \frac{\partial^3 T}{\partial x^3} + \frac{4}{77}(\text{Pr}-\frac{5}{4})\text{Pr}\rho^3 T^2 u_x \frac{\partial^3 u_x}{\partial x^3} \right. \\ -\frac{18}{77}\rho^2 T \frac{\partial^2 T}{\partial x^2} \left[\rho(\text{Pr}^2-\frac{100}{9}\text{Pr}+\frac{25}{9}) \frac{\partial T}{\partial x} + \frac{4}{9}T(\text{Pr}^2-4\text{Pr}+\frac{25}{16}) \left(\frac{\partial \rho}{\partial x} \right) - \frac{5}{9}\text{Pr}(\text{Pr}+\frac{3}{10})\rho u_x \frac{\partial u_x}{\partial x} \right] \\ +\frac{2}{7}\text{Pr}\rho^2 T \left[\rho u_x (\text{Pr}-\frac{1}{2}) \frac{\partial T}{\partial x} + \frac{50}{33}[\frac{3}{25}(\text{Pr}-\frac{5}{4})u_x \frac{\partial \rho}{\partial x} + \rho \frac{\partial u_x}{\partial x} (\text{Pr}-\frac{22}{25})]T \right] \frac{\partial^2 u_x}{\partial x^2} \\ -\frac{26}{77}\rho T^2 \left[\rho(\text{Pr}^2-\frac{2}{13}\text{Pr}+\frac{25}{52}) \frac{\partial T}{\partial x} + \frac{2}{13}\text{Pr}^2(\rho u_x \frac{\partial u_x}{\partial x} - 2\frac{\partial \rho}{\partial x}T) \right] \frac{d^2 \rho}{dx^2} + \frac{4}{77}\text{Pr}^2 \rho^2 T^3 \frac{\partial^3 \rho}{\partial x^3} \\ +\rho^3 (\text{Pr}-\frac{25}{154}) \left(\frac{\partial T}{\partial x} \right)^3 + \frac{2}{11} \left[-\frac{9}{7}T(\text{Pr}^2-\frac{85}{18}\text{Pr}+\frac{25}{18}) \frac{\partial \rho}{\partial x} + \text{Pr}(\text{Pr}+\frac{3}{14})\rho u_x \frac{\partial u_x}{\partial x} \right] \rho^2 \left(\frac{\partial T}{\partial x} \right)^2 \\ +\frac{62}{77} \left[\left(\frac{11\text{Pr}^2}{31} + \frac{25}{124} \right) T \left(\frac{\partial \rho}{\partial x} \right)^2 + \frac{5\text{Pr}}{31} \frac{\partial u_x}{\partial x} (\text{Pr}+\frac{3}{10})\rho u_x \frac{\partial \rho}{\partial x} + \text{Pr}\rho^2 (\text{Pr}-\frac{14}{93}) \left(\frac{\partial u_x}{\partial x} \right)^2 \right] \rho T \left(\frac{\partial T}{\partial x} \right) \\ \left. -\frac{4\text{Pr}^2}{231}T \left[\rho^3 u_x \left(\frac{\partial u_x}{\partial x} \right)^3 - 3\rho^2 T \frac{\partial \rho}{\partial x} \left(\frac{\partial u_x}{\partial x} \right)^2 - 3\rho T u_x \frac{\partial u_x}{\partial x} \left(\frac{\partial \rho}{\partial x} \right)^2 + 3T^2 \left(\frac{\partial \rho}{\partial x} \right)^3 \right] \right\}$
Δ_3^*	flux of Δ_2^*	$\Delta_3^{*(1)} = -3\tau\rho T \frac{\partial T}{\partial x} - \frac{6}{5}(\text{Pr}-1)\Delta_{3,1}^{*(1)}$ $\Delta_3^{*(2)} = \frac{8}{\text{Pr}}\tau^2\rho T \left[\frac{1}{2}(\text{Pr}-\frac{1}{2})T \frac{\partial^2 u_x}{\partial x^2} + (\text{Pr}+\frac{1}{4}) \frac{\partial T}{\partial x} \frac{\partial u_x}{\partial x} \right] - \frac{6}{5}(\text{Pr}-1)\Delta_{3,1}^{*(2)}$
Δ_4^*	flux of Δ_3^*	$\Delta_4^{*(1)} = -8\tau\rho T^2 \frac{\partial u_x}{\partial x}$ $\Delta_4^{*(2)} = \frac{38}{\text{Pr}}\tau^2 \left\{ -\frac{4}{19}(\text{Pr}-\frac{5}{2})\rho T^2 \frac{\partial^2 T}{\partial x^2} - \frac{4}{19}\text{Pr}T^3 \frac{\partial^2 \rho}{\partial x^2} + \frac{4}{19}\text{Pr} \left(\frac{\partial \rho}{\partial x} \right)^2 \frac{T^3}{\rho} \right. \\ \left. -\frac{4}{19}(\text{Pr}-1)T^2 \frac{\partial T}{\partial x} \frac{\partial \rho}{\partial x} + \rho T \left[\frac{4}{19}\text{Pr}T \left(\frac{\partial u_x}{\partial x} \right)^2 + \left(\frac{\partial T}{\partial x} \right)^2 \right] \right\}$
Δ_5^*	flux of Δ_4^*	$\Delta_5^{*(1)} = 40\tau\rho T u_x \left(\frac{1}{3}u_x^2 + T \right) \frac{\partial u_x}{\partial x} - 30 \left[\frac{\partial T}{\partial x} \tau\rho T + \frac{2}{5}(\text{Pr}-1)\Delta_{3,1}^{*(1)*} \right] (u_x^2 + T)$ $\Delta_5^{*(2)} = \frac{120}{\text{Pr}}\tau^2 \left[\frac{1}{3}(\text{Pr}-\frac{1}{2})\rho T^3 \frac{\partial^2 u_x}{\partial x^2} + (\text{Pr}+\frac{1}{2})\rho T^2 \frac{\partial u_x}{\partial x} \frac{\partial T}{\partial x} \right] - 12(\text{Pr}-1)T\Delta_{3,1}^{*(2)}$
$\Delta_{4,2}^*$	flux of $\Delta_{3,1}^*$	$\Delta_{4,2}^{*(1)} = -\frac{14}{3}\tau\rho T^2 \frac{\partial u_x}{\partial x}$ $\Delta_{4,2}^{*(2)} = \frac{77}{3\text{Pr}}\tau^2 \left\{ -\frac{2}{11}(\text{Pr}-\frac{19}{7})\rho T \frac{\partial^2 T}{\partial x^2} - \frac{2\text{Pr}}{11}T^2 \frac{\partial^2 \rho}{\partial x^2} + \frac{2\text{Pr}}{11} \frac{T^2}{\rho^2} \left(\frac{\partial \rho}{\partial x} \right)^2 \right. \\ \left. -\frac{2}{11}(\text{Pr}-1)T \frac{\partial T}{\partial x} \frac{\partial \rho}{\partial x} + \rho T \left[\frac{6T}{77} \left(\frac{\partial u_x}{\partial x} \right)^2 \text{Pr} + \left(\frac{\partial T}{\partial x} \right)^2 \right] \right\}$
$\Delta_{5,3}^*$	flux of $\Delta_{4,2}^*$	$\Delta_{5,3}^{*(1)} = -21\tau\rho T^2 \frac{\partial T}{\partial x} - \frac{42}{5}(\text{Pr}-1)T\Delta_{3,1}^{*(1)}$ $\Delta_{5,3}^{*(2)} = \frac{72}{\text{Pr}}\tau^2 \left[\frac{11}{36}(\text{Pr}-\frac{7}{11})\rho T^3 \frac{\partial^2 u_x}{\partial x^2} + \rho T^2 (\text{Pr}+\frac{5}{12}) \frac{\partial u_x}{\partial x} \frac{\partial T}{\partial x} \right] - \frac{42}{5}(\text{Pr}-1)T\Delta_{3,1}^{*(2)}$
$\Delta_{6,4}^*$	flux of $\Delta_{5,3}^*$	$\Delta_{6,4}^{*(1)} = -36\tau\rho T^3 \frac{\partial u_x}{\partial x}$ $\Delta_{6,4}^{*(2)*} = \frac{441}{\text{Pr}}\tau^2 \left\{ -\frac{4}{49}(\text{Pr}-\frac{25}{6})\rho T^3 \frac{\partial^2 T}{\partial x^2} - \frac{4\text{Pr}}{49}T^4 \frac{\partial^2 \rho}{\partial x^2} + \frac{4\text{Pr}}{49} \frac{T^4}{\rho} \left(\frac{\partial \rho}{\partial x} \right)^2 \right. \\ \left. -\frac{4}{49}(\text{Pr}-1)T^3 \frac{\partial T}{\partial x} \frac{\partial \rho}{\partial x} + \rho T^2 \left[\frac{68}{441}\text{Pr}T \left(\frac{\partial u_x}{\partial x} \right)^2 + \left(\frac{\partial T}{\partial x} \right)^2 \right] \right\}$

Table 2: Analytical expressions for various orders of TNE quantities.

$$\frac{\partial \rho u_x}{\partial t_1} + \frac{\partial(\rho u_x u_x + \rho RT)}{\partial x} = 0, \quad (28)$$

$$\frac{\partial e}{\partial t_1} + \frac{\partial(eu_x + \rho RTu_x)}{\partial x} = 0, \quad (29)$$

where $e = \rho(\frac{1+n}{2}RT + \frac{1}{2}u_x^2)$ represents the total energy density of the fluid.

In the above derivation, the first five kinetic moments, $M_0(f^{eq})$, $M_1(f^{eq})$, $M_2(f^{eq})$, $M_{2,0}(f^{eq})$ and $M_{3,1}(f^{eq})$, are needed. Their expressions are as follows:

$$M_0(f^{eq}) = \int f^{eq} dv_x d\eta = \rho, \quad (30)$$

$$M_1(f^{eq}) = \int f^{eq} v_x dv_x d\eta = \rho u_x, \quad (31)$$

$$M_{2,0}(f^{eq}) = \int \frac{1}{2} f^{eq} (v_x^2 + \eta^2) dv_x d\eta = \frac{1}{2} \rho [(1+n)RT + u_x^2], \quad (32)$$

$$M_2(f^{eq}) = \int f^{eq} v_x v_x dv_x d\eta = \rho(RT + u_x^2), \quad (33)$$

$$M_{3,1}(f^{eq}) = \int \frac{1}{2} f^{eq} v_x (v_x^2 + \eta^2) dv_x d\eta = \frac{1}{2} \rho u_x [(n+3)RT + u_x^2]. \quad (34)$$

From CE analysis, incorporating all orders of TNE effects into Eqs. (27) to (29), yields the completed hydrodynamic equations

$$\frac{\partial \rho}{\partial t_1} + \frac{\partial(\rho u_x)}{\partial x} = 0, \quad (35)$$

$$\frac{\partial \rho u_x}{\partial t_1} + \frac{\partial(\rho u_x u_x + \rho RT)}{\partial x} + \frac{\partial \Delta_2}{\partial x} = 0, \quad (36)$$

$$\frac{\partial e}{\partial t_1} + \frac{\partial(eu_x + \rho RTu_x)}{\partial x} + \frac{\partial \Delta_{3,1}}{\partial x} = 0. \quad (37)$$

where Δ_2 and $\Delta_{3,1}$ are the thermo-hydrodynamic non-equilibrium (THNE) quantities. Their expressions are

$$\Delta_2 = \int (f^{(1)} + f^{(2)} + \dots + f^{(k)}) v_x^2 dv_x d\eta, \quad (38)$$

and

$$\Delta_{3,1} = \int \left[(f^{(1)} + f^{(2)} + \dots + f^{(k)}) \frac{v_x^2 + \eta^2}{2} \right] v_x dv_x d\eta. \quad (39)$$

Unlike Δ_m^* and $\Delta_{m,n}^*$ which solely measure the TNE effects, Δ_m and $\Delta_{m,n}$ represent the combined effects of HNE and TNE.

When considering only the first-order Kn number effects, the generalized hydrodynamic equations, Eqs. (35) to (37), reduce to the NS equations, with linear constitutive relations, $\Delta_2 = \Delta_2^{(1)} = \Delta_2^{*(1)}$ and $\Delta_{3,1} = \Delta_{3,1}^{(1)} = \Delta_{3,1}^{*(1)} + u_x \Delta_2^{*(1)}$. When the second-order Kn number effects are preserved, the nonlinear constitutive relations in the Burnett equations are: $\Delta_2 = \Delta_2^{(1)} + \Delta_2^{(2)} = \Delta_2^{*(1)} + \Delta_2^{*(2)}$ and $\Delta_{3,1} = \Delta_{3,1}^{(1)} + \Delta_{3,1}^{(2)} = \Delta_{3,1}^{*(1)} + \Delta_{3,1}^{*(2)} + u_x \Delta_2^{*(1)} + u_x \Delta_2^{*(2)}$. For the third-order case, the nonlinear constitutive relations in the super-Burnett equations are: $\Delta_2 = \Delta_2^{(1)} + \Delta_2^{(2)} + \Delta_2^{(3)}$ and $\Delta_{3,1} = \Delta_{3,1}^{(1)} + \Delta_{3,1}^{(2)} + \Delta_{3,1}^{(3)}$. The derivation of TNE quantities is provided in Section 3.3.

3.2. Distribution functions

From Eqs. (27) to 29, the temporal derivatives of the macroscopic quantities can be expressed in terms of spatial derivatives.

$$\frac{\partial \rho}{\partial t_1} = -u_x \frac{\partial \rho}{\partial x} - \rho \frac{\partial u_x}{\partial x}, \quad (40)$$

$$\frac{\partial u_x}{\partial t_1} = -u_x \frac{\partial u_x}{\partial x} - \frac{T}{\rho} \frac{\partial \rho}{\partial x} - \frac{\partial T}{\partial x}, \quad (41)$$

and

$$\frac{\partial T}{\partial t_1} = -u_x \frac{\partial T}{\partial x} - \frac{2}{n+1} T \frac{\partial u_x}{\partial x}. \quad (42)$$

From Eq. (26), the first-order distribution function is given by

$$f^{(1)} = -\tau \left[\frac{\partial f^{eq}}{\partial t_1} + v_x \frac{\partial f^{eq}}{\partial x} \right] + f^{s(1)}, \quad (43)$$

where $f^{s(k)} = f^{eq} \left[(1 - \text{Pr}) c_x q_x^{(k)} \frac{c_x^2 + \eta^2}{(n+3)pRT} - (n+3) \right]$. Substituting Eq. (3) into Eq. (43), and replacing the temporal derivatives with spatial ones, analytical solutions of $f^{(1)}$, expressed as spatial derivatives of macroscopic quantities, are obtained.

Along this way, by extracting the second- and third-orders terms of Kn number from Eq. (25), we obtain

$$\frac{\partial f^{eq}}{\partial t_2} + \frac{\partial f^{(1)}}{\partial t_1} + v_x \frac{\partial f^{(1)}}{\partial x} = -\frac{1}{\tau} (f^{(2)} - f^{s(2)}), \quad (44)$$

and

$$\frac{\partial f^{eq}}{\partial t_3} + \frac{\partial f^{(1)}}{\partial t_2} + \frac{\partial f^{(2)}}{\partial t_1} + v_x \frac{\partial f^{(2)}}{\partial x} = -\frac{1}{\tau} (f^{(3)} - f^{s(3)}). \quad (45)$$

The second- and third-orders expressions of distribution function are given as follows:

$$f^{(2)} = -\tau \left[\frac{\partial f^{(1)}}{\partial t_1} + \frac{\partial f^{eq}}{\partial t_2} + v_x \frac{\partial f^{(1)}}{\partial x} \right] + f^{s(2)}, \quad (46)$$

and

$$f^{(3)} = -\tau \left[\frac{\partial f^{eq}}{\partial t_3} + \frac{\partial f^{(1)}}{\partial t_2} + v_x \frac{\partial f^{(2)}}{\partial x} \right] + f^{s(3)}. \quad (47)$$

3.3. TNE measures

By integrating the distribution functions $f^{(k)}$ over their velocity and η spaces, higher-order TNE quantities can be defined as:

$$\Delta_m^{*(k)} = \int f^{(k)} c_x^2 dv_x d\eta, \quad (48)$$

and

$$\Delta_{m,n}^{*(k)} = \int \left[f^{(k)} \frac{c_x^2 + \eta^2}{2} \right] c_x dv_x d\eta. \quad (49)$$

For convenience, the analytical expressions for different orders of TNE quantities are listed in Table 2. Specifically, expressions for the first-order to third-order terms of $\Delta_{3,1}^*$ are given, while only the first-order and second-order expressions are provided for the other TNE quantities. Additionally, the results in Table 2 correspond to the case where $n = 2$.

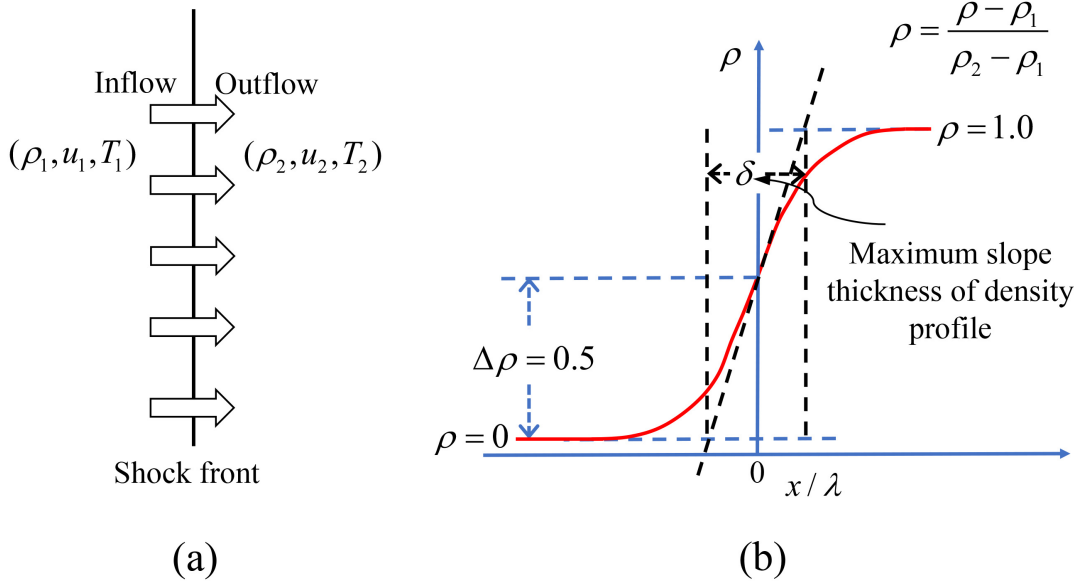


Figure 1: (a) Schematic representation of flows on both sides of the shock front. (b) Schematic of the normalized density profile within the shock's internal structure.

4. DBM simulation and numerical results

4.1. Shock wave configuration

In this section, we analyze the effects of the Mach number on non-equilibrium characteristics, including both HNE and TNE effects, using the constructed Shakov-DBM. Figures 1(a) illustrates the configurations of macroscopic quantities, while Figure 1(b) shows the density profile of the internal structure of the shock when it has evolved to a steady state. From Figure 1(b), the following observations can be made: (i) The position corresponding to a normalized density of $\tilde{\rho} = 0.5$ is set as the origin of the horizontal axis. (ii) The parameter δ represents the maximum slope thickness of the density profile, which serves as an approximate measure of the shock's internal structure thickness [26].

The macroscopic quantities on either side of the shock front satisfy the Rankine-Hugoniot relations, expressed as,

$$\rho_2 = \rho_1 \cdot a, \quad (50)$$

$$T_2 = T_1 \cdot b/a, \quad (51)$$

and

$$u_2 = u_1/a. \quad (52)$$

where $a = \gamma_1 \cdot \text{Ma}^2 / (2.0 + \gamma_{-1} \cdot \text{Ma}^2)$ and $b = 2.0 \cdot \gamma \cdot \text{Ma}^2 / \gamma_1 - \gamma_{-1} / \gamma_1$, with $\gamma_{-1} = \gamma - 1$ and $\gamma_1 = \gamma + 1$. For argon gas, the specific heat ratio is $\gamma = 5/3$.

4.2. Molecular interaction models

Macroscopic transport characteristics of flows arise from the collective effects of microscopic molecular collisions. Consequently, different molecular interaction models can yield distinct transport behaviors. To facilitate comparison, two molecular models are discussed below.

The first model is the variable hard-sphere (VHS) model, which incorporates an inverse power law for intermolecular forces. In this model, the collision frequency (the inverse of the collision relaxation time) between molecules is given by [74]:

$$\hat{\nu} = \frac{16}{5} \sqrt{\frac{R}{2\pi}} \frac{T_\infty^{\chi-1/2}}{\rho_\infty} \frac{\hat{\rho}}{T^{\chi-1}} \frac{1}{\lambda_\infty}, \quad (53)$$

where χ represents the temperature dependence of viscosity. Physical quantities marked with “ ∞ ” and “ $\hat{}$ ” represent reference values and real physical quantities, respectively. λ_∞ denotes the average free path of molecules.

The second model combines the VHS model with the variable soft-sphere (VSS) model [52, 53], and is expressed as:

$$\hat{\nu} = \frac{4\alpha(5-2\omega)(7-2\omega)}{2(\alpha+1)(\alpha+2)} \sqrt{\frac{R}{2\pi}} \frac{T_\infty^{\chi-1/2}}{\rho_\infty} \frac{1}{\lambda_\infty} \frac{\hat{\rho}}{\hat{T}^{\chi-1}}, \quad (54)$$

where ω and α are indices for the VHS and VSS models, respectively. Their values depend on the gas type and state.

Before performing the simulation, it is essential to nondimensionalize Eqs. (53) and (54). By substituting the reference velocity $c_\infty = \sqrt{RT_\infty}$ into these equations, the dimensionless collision frequency becomes:

$$\nu = \frac{16}{5\sqrt{2\pi}\text{Kn}} \rho T^{1-\chi}, \quad (55)$$

and

$$\nu = \frac{4\alpha(5-2\omega)(7-2\omega)}{5(\alpha+1)(\alpha+2)} \cdot \frac{1}{\sqrt{2\pi}\text{Kn}} \rho T^{1-\chi}, \quad (56)$$

where $\text{Kn} = \lambda_\infty / L_\infty$. To capture the internal structure of a shock, the averaged free path is typically taken as the characteristic L_∞ , i.e., $L_\infty = \lambda_\infty$. Under this condition, the Kn number is $\text{Kn} = 1$.

Ma number	molecular model	dt	α, ω, χ
1.2, 1.4	VHS-VSS	0.001	$\alpha = 1.4, \omega = 0.81, \chi = 0.81$
1.55 - 2.5			$\chi = 0.81$
3.8 - 6.0		0.0005	$\chi = 0.81$
8.0	VHS		$\chi = 0.75$
9.0		0.0001	$\chi = 0.72$
10.0			$\chi = 0.71$

Table 3: Parameters used in the simulation of shock waves with various Ma numbers.

In the subsequent simulations, the second model is used for cases with $Ma = 1.2$ and $Ma = 1.4$, while the first is applied to the other Ma numbers.

4.3. Numerical schemes and parameter settings

This paper continues the direct discretization of particle velocity space as presented in the Ref. [70]. The velocity space, ranging from $-v_{max}$ to v_{max} , is divided non-uniformly, with v_{max} representing the truncation velocity. The discrete method is given by

$$v_i = \left(i - \frac{N_{vx} + 1}{2}\right)^\lambda / \left(\frac{N_{vx} - 1}{2}\right)^\lambda v_{max} + v_0, \quad (57)$$

where i represents the index of grid points in the velocity space, and N_{vx} denotes the total number of grids. The parameter λ is a positive odd number that refines the velocity space near the initial velocity v_0 . The difference between two adjacent velocity grids is expressed as

$$\delta v(i) = \frac{\lambda}{\left(i - \frac{N_{vx} + 1}{2}\right)(v_i - v_0)}. \quad (58)$$

To numerically solve Eq. (4), appropriate numerical schemes are required for both temporal and spatial derivatives. In this study, we use the first-order forward Euler finite difference scheme for the time derivative and the fifth-order weighted essentially non-oscillatory (WENO) scheme for the spatial derivative. Both schemes have been extensively validated in previous literature.

Shock waves with Mach numbers ranging from 1.2 to 10.0 are simulated. The spatial domain, spanning from 0 to $200 \cdot \lambda$, is divided into 1000 grid points, resulting in a dimensionless grid size of $\Delta x = 0.2$. The parameters for discretizing the velocity space are as follows: $v_{max} = 50.0$, $N_{vx} = 300$, and $\lambda = 5.0$. For argon gas, the degrees of freedom is $n = 2$, leading to $\gamma = 5/3$. The Prandtl number for argon is $2/3$. Other dimensionless parameters depend on the gas state, as summarized in Table 3.

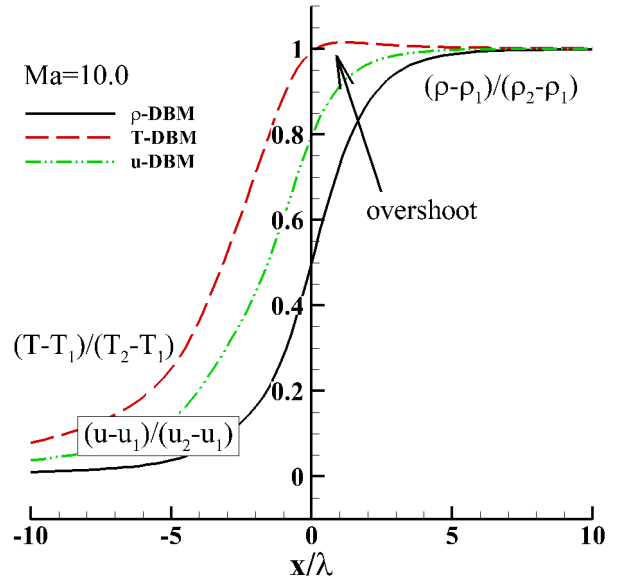


Figure 2: The normalized density, velocity and temperature profiles of a shock for $Ma = 10.0$.

4.4. Internal structure of a shock

For clarity, Fig. 2 shows the DBM numerical results for normalized density, velocity, and temperature profiles of a shock with a Mach number of 10.0. The following observations can be made:

(I) The positions of the three interfaces do not coincide, with a separation of several λ .

(II) The temperature interface is located at the front of the shock, followed by the velocity and density interfaces, respectively.

(III) The shapes of the three interfaces differ in terms of slope, thickness, and symmetry. Notably, the temperature overshoot is pronounced at high Mach numbers, while the velocity and density interfaces do not exhibit such an overshoot.

The impact of these differences in the internal interfaces of the shock on flow behavior, essentially governed by different TNE quantities, warrants further investigation.

4.5. Comparison with DSMC and experimental results

Figure 3 compares the density and temperature profiles inside the shocks from DBM simulations with other results. The profiles for shock waves with Mach numbers ranging from 1.2 to 9.0 are shown. The DBM simulation results closely match those from DSMC simulations and experimental data, demonstrating that the DBM model accurately captures the internal structures of shock waves, even at high Mach numbers.

Additionally, a temperature overshoot begins to appear as the Mach number approaches 3.8. As the Mach number increases to 8.0, the temperature overshoot becomes more pronounced. This overshoot is a typical nonequilibrium phenomenon caused by the rapid accumulation of heat without sufficient time for dissipation. Shan *et al.* investigated the mechanism behind the temperature overshoot, attributing it to higher-order TNE effects [75].

4.6. Effects of Mach number on macroscopic quantities

4.6.1. Two-stage Effects on shock shapes and compressibility

To investigate the effects of Mach number on macroscopic quantities within the shock structure, Fig. 4 presents the DBM simulation results for the density (first row), temperature (second row), and velocity (third row) profiles. The left and right columns correspond to cases with lower and higher Mach numbers, respectively.

For the density profiles, the effects of the Mach number are two-stage. Specifically, a critical Mach number, Ma_ρ ($Ma_\rho \approx 3.8$), separates two distinct behaviors. When $Ma < Ma_\rho$, as shown in Fig. 4(a), the Mach number steepens the interface. Conversely, for $Ma > Ma_\rho$, as shown in Fig. 4(b), the interface becomes gentler. Additionally, for $Ma < Ma_\rho$, the density profiles are more diffuse near the outflow region and more compact near the inflow region. Beyond the critical value ($Ma > Ma_\rho$), this trend reverses. In summary, when $Ma < Ma_\rho$, the Mach number primarily sharpens the interface, while for $Ma > Ma_\rho$, it broadens the interface.

This phenomenon is primarily due to the compressibility of the fluid inside the shock. When the Mach number is below

Ma_ρ , the shock is weaker, and the fluid's compressibility is stronger, particularly in the region ahead of the shock, where the fluid undergoes significant compression. This compression amplifies changes in physical quantities across the shock, resulting in a steeper interface gradient. In this case, the density distribution exhibits larger variations near the outflow region and a more compact arrangement near the inflow region. When the Mach number exceeds Ma_ρ , the compressibility weakens, the compression effect saturates, and the changes in physical quantities across the shock become smoother. The transition region of the shock broadens, and the density distribution smooths, producing a gentler shock interface.

The effects of Mach number on temperature and velocity interfaces also exhibit two-stage behavior. Taking the temperature profiles as an example, an intersection occurs when $Ma < Ma_T$ [$Ma_T \approx 2.5$, see Fig. 4(c)], but no intersection is observed for $Ma > Ma_T$ [see Fig. 4(d)]. Similar to the density profiles, the temperature profiles near the outflow region are more diffuse for $Ma < Ma_T$ and more compact for $Ma > Ma_T$. This phenomenon indicates that, as the Mach number increases, the region with strong compressibility in the fluid shifts from the near-outflow region to the near-inflow region.

4.6.2. Effects of Mach number on shock thickness

To quantitatively characterize the thickness of the shock structure, the maximum slope thickness [see Fig. 1(b)] is defined. Figure 5 illustrates the thicknesses of the density, temperature, and velocity interfaces obtained from DBM simulations. For comparison, experimental results for density interface thicknesses are also included. Across the Mach number range from 1.1 to 9.0, the DBM simulation results align with the experimental data, staying within the error margins. However, when $Ma > 9$, the discrepancy between the simulation and experimental results gradually increases.

The effects of Mach number on interface thicknesses also exhibit two-stage behavior. As Mach number increases, the thicknesses of all three interfaces first increase sharply and then decrease gradually, reaching their maximum at critical Mach numbers. The critical Mach numbers for the three types of interfaces differ. Specifically, they are $Ma_\rho \approx 3.8$, $Ma_T \approx 2.5$, and $Ma_u \approx 2.5$, respectively, consistent with results in Fig. 4.

Key observations include: (i) For $Ma < 2.0$, the thicknesses of all three interfaces are nearly identical. (ii) For $Ma > 2.0$, the density interface thickness becomes greater than those of the velocity and temperature interfaces. As Ma increases, the gap between the density interface and the other two interfaces widens. This is because density changes are more directly influenced by compression effects, leading to a faster growth rate for the density interface thickness compared to the velocity and temperature interfaces. (iii) For $Ma < 3.8$, the temperature interface thickness exceeds that of the velocity interface, but this trend reverses for $Ma > 3.8$.

Each interface exhibits distinct structural features and driving mechanisms. The density interface reflects the compressibility of the fluid, making it the most affected by shock compression effects. In contrast, temperature changes depend more on thermal conduction than compressibility. As the Mach number in-

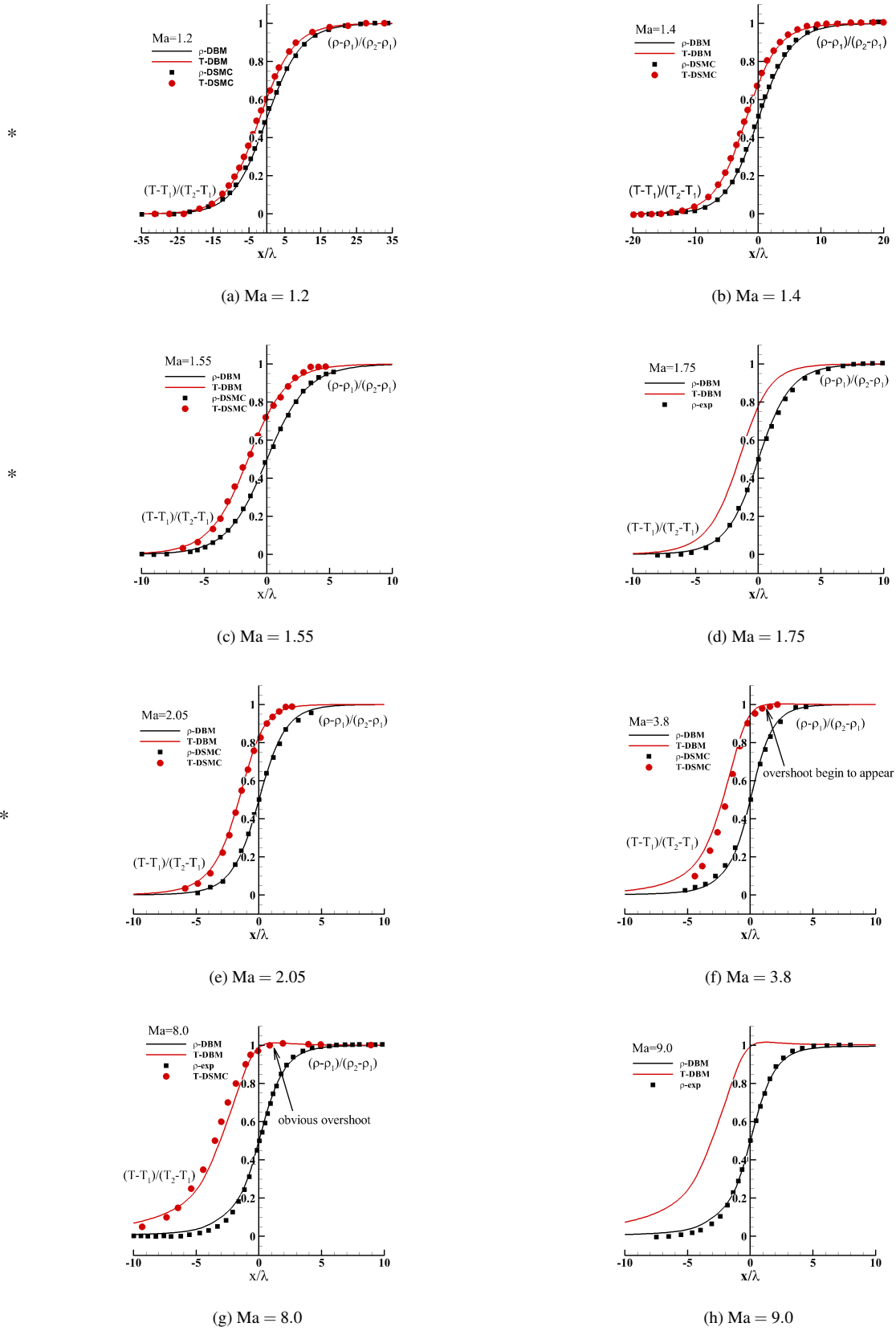
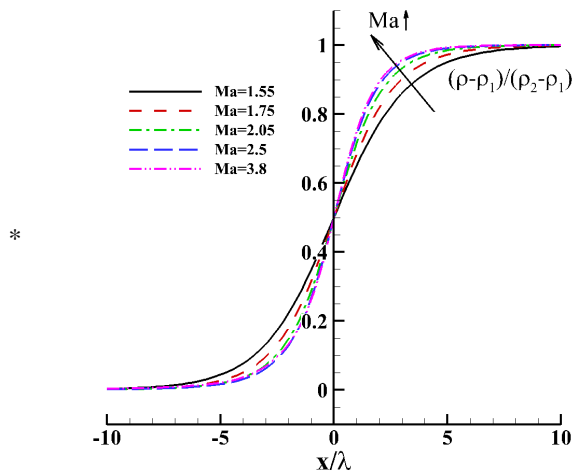
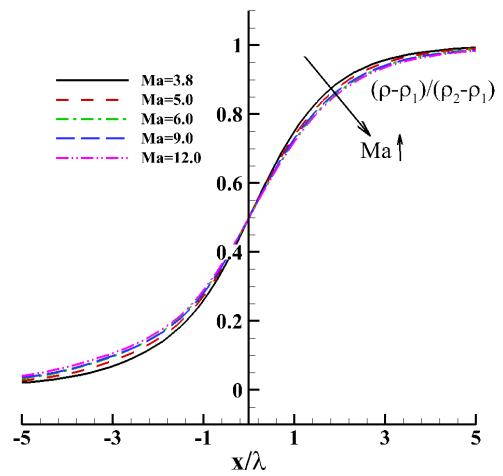


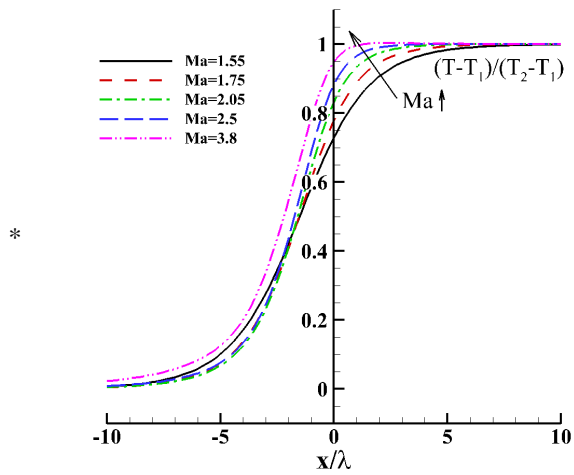
Figure 3: Comparisons of shock structure between DBM simulation and DSMC (or experimental) results. The DSMC results for $Ma = 1.2$ and 1.4 are obtained from Fig. 3 in the Ref. [74]. The DSMC and experimental data for $Ma = 1.55$ to 9.0 are from the Ref. [26]. Among these, the DSMC results for $Ma = 1.55, 2.05,$ and 3.8 are from Fig. 5. The experimental data sources are: $Ma = 1.75$ from Fig. 3, $Ma = 8.0$ from Fig. 7, and $Ma = 9.0$ from Fig. 4, respectively.



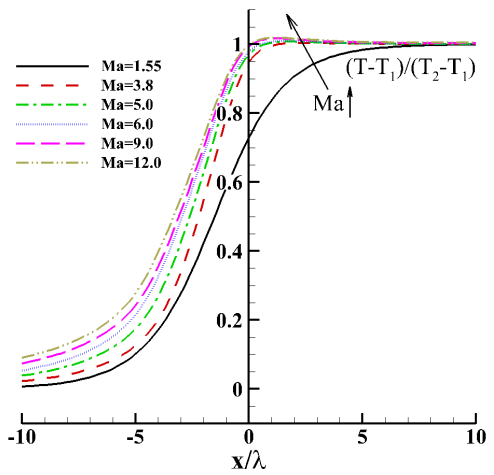
(a) Ma = 1.55 ~ 3.8



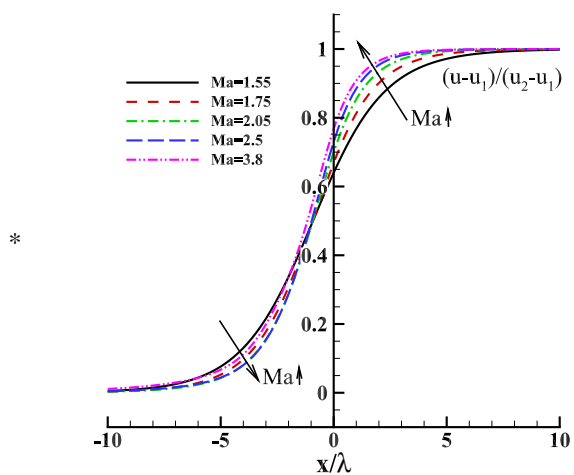
(b) Ma = 3.8 ~ 12.0



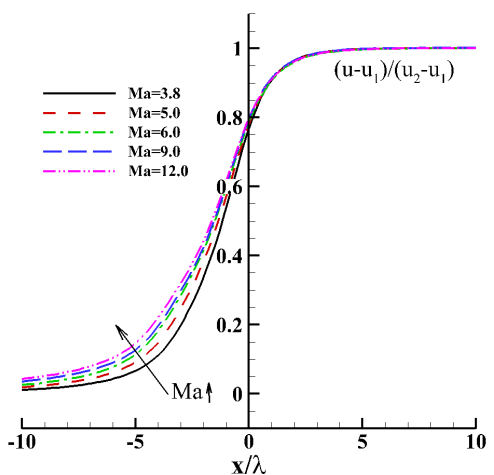
(c) Ma = 1.55 ~ 3.8



(d) Ma = 1.55, 3.8 ~ 12.0



(e) Ma = 1.55 ~ 3.8



(f) Ma = 3.8 ~ 12.0

Figure 4: DBM simulation results of density, temperature, and velocity profiles, respectively.

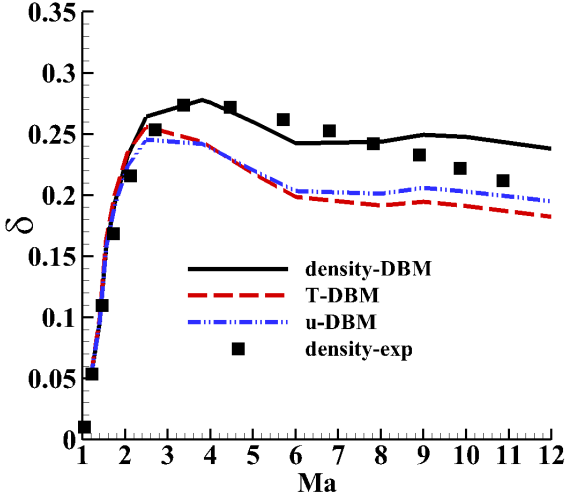


Figure 5: Thicknesses of various types of interfaces. The experimental data are taken from Fig. 2 in Ref. [26].

creases, the time for fluid to pass through the shock decreases, limiting the time available for heat diffusion. This weakens the thermal conduction effect, resulting in a relatively smaller temperature interface thickness. The velocity interface is primarily influenced by viscous effects. As the Mach number increases, the velocity gradient within the shock steepens. However, the shorter transit time across the shock limits the relaxation time required for viscous effects to fully smooth the velocity gradient. For compressible flows, changes in density, temperature, and velocity interfaces are interconnected. These effects combine to create maximum interface thickness at critical Mach numbers, corresponding to the strong nonequilibrium state of the shock.

4.7. Effects of Ma number on distribution function

In kinetic methods, nonequilibrium effects are reflected not only macroscopically in the spatio-temporal gradients of macroscopic quantities, such as constitutive relations, but also mesoscopically in the distribution function. Analyzing the characteristics of the distribution function is essential for model selection and provides insights into both HNE and TNE phenomena. As mentioned in Section 2.2, directly discretizing the velocity space enables DBM models to accurately capture higher-order TNE effects. This approach also facilitates the direct acquisition of the true distribution functions. However, a significant challenge of this method is identifying which order of TNE dominates in practical simulations.

To address this issue, CE analysis is often employed to systematically increase the degree of non-equilibrium. The CE analysis provides analytical expressions for distribution functions at different TNE orders, enabling a more comprehensive understanding of the dominant nonequilibrium effects. For example, as shown in Section 3, the first three orders of the distri-

bution function g are:

$$g^{(1)} = -\tau \left[\frac{\partial g^{eq}}{\partial t_1} + v_x \cdot \frac{\partial g^{eq}}{\partial x} \right] + g^{s(1)}, \quad (59)$$

$$g^{(2)} = -\tau \left[\frac{\partial g^{(1)}}{\partial t_1} + \frac{\partial g^{eq}}{\partial t_2} + v_x \cdot \frac{\partial g^{(1)}}{\partial x} \right] + g^{s(2)}, \quad (60)$$

and

$$g^{(3)} = -\tau \left[\frac{\partial g^{eq}}{\partial t_3} + \frac{\partial g^{(1)}}{\partial t_2} + v_x \cdot \frac{\partial g^{(2)}}{\partial x} \right] + g^{s(3)}, \quad (61)$$

where

$$g^{s(k)} = g^{eq} + g^{eq} \left\{ (1 - \text{Pr}) \cdot c_x q_x^{(k)} \cdot \frac{[\frac{c_x^2}{RT} - 3]}{[(n+3)pRT]} \right\}. \quad (62)$$

It is worth noting that the term $\frac{\partial g^{(2)}}{\partial t_1} = 0$, as changes in $g^{(2)}$ cannot be observed on the t_1 time scale. Otherwise, the zeroth, first, and second contracted moments of $g^{(3)}$ would be nonzero, violating the conservation laws [76].

To analyze non-equilibrium states within the shock, Fig. 6 compares the distribution functions g obtained from DBM simulations with analytical results of various accuracy orders. For Mach numbers ranging from 1.4 to 2.5, distribution functions are evaluated at positions across the internal structure, spanning from the inflow to outflow regions. Specifically, five positions with normalized densities $\tilde{\rho} = 0.1, 0.3, 0.5, 0.7$ and 0.9 , are considered, respectively. Larger (smaller) normalized density values $\tilde{\rho}$ indicate positions closer to the outflow (inflow) region. Black lines represent the equilibrium distribution function $g^{(0)}$. Red points are BM simulation results with g preserving sufficient non-equilibrium orders. Pink ($g^{(1)}$), green ($g^{(1)} + g^{(2)}$) and blue ($g^{(1)} + g^{(2)} + g^{(3)}$) lines denote analytical solutions considering up to the first-order, second-order, and third-order TNE, respectively.

4.7.1. Appearances of distribution function

Several key observations can be made:

(I) For $Ma = 1.4$, as shown in Fig. 6(a), the distribution function is non-zero within $v_x = (-2, 4)$, and zero outside this range. As the Mach number increases, the non-zero region of the distribution function expands, compared to cases with lower Mach numbers.

(II) As $\tilde{\rho}$ increases (i.e., closer to the outflow), the values of the distribution function increase due to the corresponding macroscopic quantities.

(III) The peak of the distribution function shifts towards lower particle velocities v_x as $\tilde{\rho}$ increases.

(IV) For $Ma = 1.55$, as shown in Fig. 6(b), the peak values of the distribution function are higher than those observed for $Ma = 1.4$. As the Mach number further increases, the peak values of the distribution function gradually rise. Interestingly, for $Ma = 3.8$ [see Fig. 6(a)], the peak values of the distribution function are significantly lower than those observed at smaller Mach numbers. This suggests that the influence of Mach number on the distribution function exhibits a two-stage effect, similar to its impact on macroscopic quantity interfaces. For more details, refer to Sec. 4.7.3.

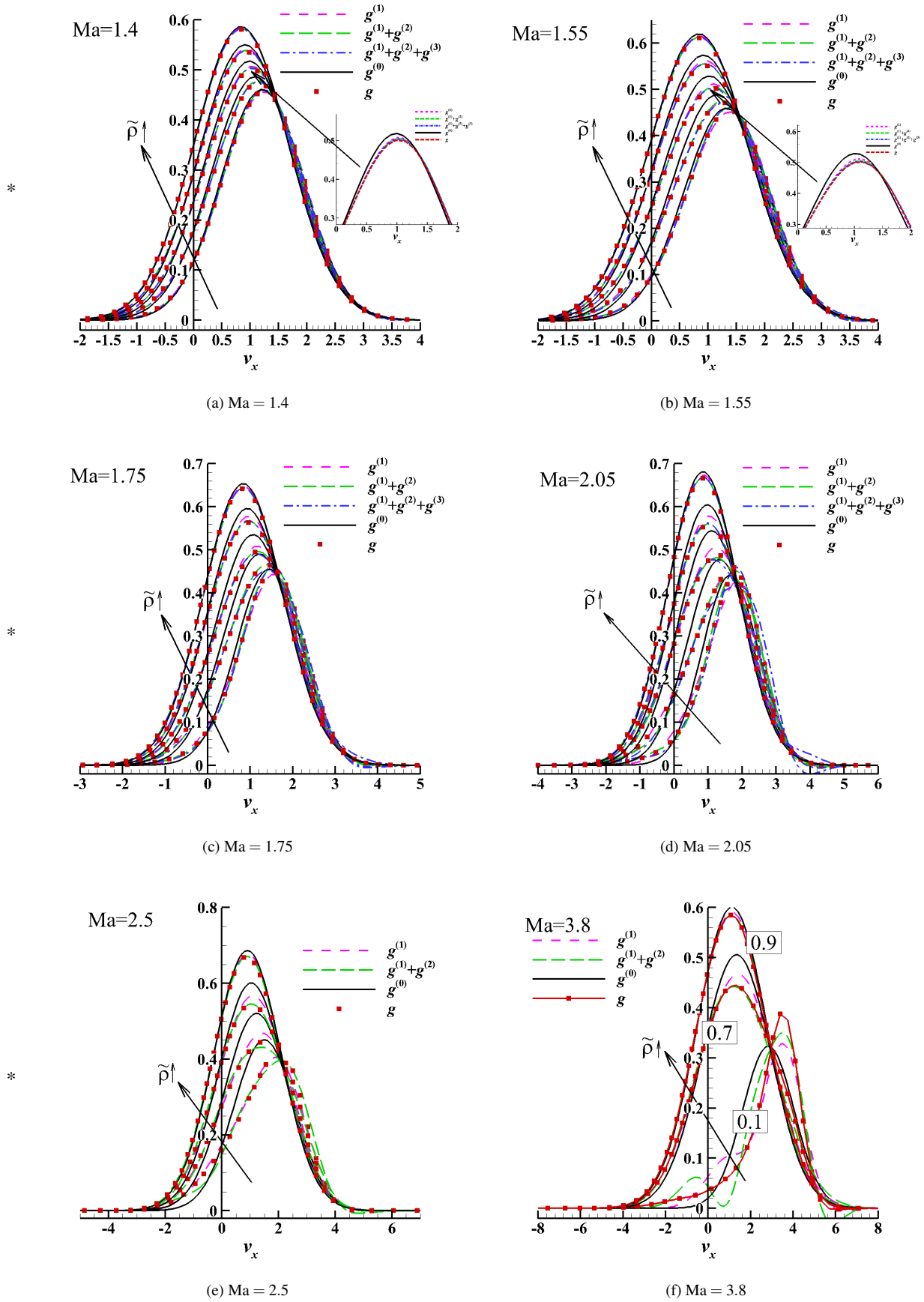


Figure 6: Comparisons of distribution functions between DBM simulation and analytical solutions inside the shock structure.

4.7.2. Non-equilibrium degree from perspective of distribution function

In the case of $Ma = 1.4$ [see Fig. 6(a)], the following observations can be made:

(I) At $\tilde{\rho} = 0.1$ and 0.9 , the system is near equilibrium, while intermediate positions ($\tilde{\rho} = 0.3, 0.5, 0.7$) deviate from equilibrium.

(II) The strongest TNE occurs at $\tilde{\rho} \approx 0.5$ and gradually weakens towards both ends. The location with the greatest degree of TNE is determined collectively by density, temperature, and velocity gradients, rather than solely by the density gradients.

(III) At the intermediate positions $\tilde{\rho} = 0.3, 0.5$, and 0.7 , the distribution functions, including first-order, second-order, and third-order TNE effects, align closely with the DBM results. This suggests that the fluid's deviation from equilibrium is predominantly first-order.

(IV) The subfigure showing an enlarged view of the distribution functions around the peak at $\tilde{\rho} = 0.5$ reveals that incorporating higher-order TNE effects brings the analytical results closer to the DBM simulation. This demonstrates the enhanced physical accuracy of higher-order analytical solutions.

For $Ma = 1.55$ [see Fig. 6(b)], the following observations are made:

(I) The positions at $\tilde{\rho} = 0.1$ and 0.9 are near equilibrium, while the positions at $\tilde{\rho} = 0.3, 0.5$, and 0.7 deviate from equilibrium. However, the deviations between $g^{(0)}$ and other results are more pronounced compared to the case with $Ma = 1.4$.

(II) At $\tilde{\rho} = 0.1$, the deviation from equilibrium is greater for $Ma = 1.55$ than for $Ma = 1.4$. Despite these differences, the fluid still exhibits primarily a first-order deviation from equilibrium, consistent with the observations for $Ma = 1.4$.

For $Ma = 1.75$, as shown in Fig. 6(c), the fluid at all five positions clearly exhibits a non-equilibrium state. At positions $\tilde{\rho} = 0.1, 0.3, 0.7$, and 0.9 , only first-order deviations from equilibrium are observed. However, at $\tilde{\rho} = 0.5$, the first-order analytical distribution function $g^{(1)}$ deviates noticeably from the higher-order results, while the second-order and third-order solutions align closely. This indicates that at $\tilde{\rho} = 0.5$, the fluid exhibits a second-order deviation from equilibrium.

For $Ma = 2.05$ [see Fig. 6(d)], the TNE intensity increases compared to the previous cases. At positions $\tilde{\rho} = 0.5$ and 0.7 , the fluid exhibits second-order deviations from equilibrium. However, as spatial gradients of macroscopic quantities increase, numerical errors in the analytical solutions become more significant. As a result, third-order TNE solutions do not necessarily match the simulation results better than second-order solutions, despite their higher physical accuracy.

The second-order TNE analytical solutions align well with DBM simulation results for $Ma = 2.5$ and 3.8 at most positions, except at $\tilde{\rho} = 0.1$ for $Ma = 3.8$. However, third-order solutions (not shown here) lose accuracy due to numerical errors. Consequently, as the Mach number increases further, even the second-order analytical solution may become less effective.

A detailed analysis of the distribution function's characteristics is crucial for adjusting simulation parameters and fully capturing the TNE characteristics of the fluid. Additionally, an-

alyzing the deviation between the distribution function and the equilibrium distribution function helps determine the appropriate order for fluid models.

4.7.3. Two-stage effects on distribution functions

To further investigate the influence of Mach number on distribution functions, Fig. 7 presents the DBM simulation results for g at positions $\tilde{\rho} = 0.3, 0.5$, and 0.7 for Mach numbers ranging from 1.4 to 10.0 . The following observations can be made:

(I) The influence of Mach number on the DBM results for distribution functions exhibits a two-stage effect. Overall, as the Mach number increases, the peak value of the distribution function decreases. However, for $Ma < Ma_f$ ($Ma_f \approx 2.05$), as shown in Fig. 7(d), the peak value increases with the Mach number. This phenomenon is primarily due to the combined effects of various macroscopic quantities and their gradients.

(II) For $Ma < 2.05$, the distribution function retains a higher degree of symmetry. At $Ma = 2.5$, this symmetry is significantly reduced. When the Mach number reaches 3.8 , the distribution function clearly deviates from a normal distribution. For $Ma = 8.0$, a pronounced bimodal character emerges. In fact, the symmetry of the distribution function also serves as a coarse-grained measure of the TNE degree.

(III) As the Mach number increases, the peak of the distribution function gradually shifts toward higher particle velocities v_x . This shift is related to the increase in macroscopic velocity. Based on this property, the corresponding velocity space can be refined to ensure more accurate simulation results.

4.8. Effects of Ma number on TNE measures

In the framework of DBM, non-conserved kinetic moments of $(f - f^{eq})$ provide an effective approach for characterizing the states, modes, and amplitudes of fluids deviating from equilibrium. Figure 8 displays the TNE states within shocks for Mach numbers $Ma = 1.2, 1.4$, and 2.05 , focusing on various TNE measures, including Δ_2^* , Δ_3^* , Δ_4^* , Δ_5^* , $\Delta_{3,1}^*$, $\Delta_{4,2}^*$, $\Delta_{5,3}^*$, and $\Delta_{6,4}^*$. As illustrated, the left column represents even-order TNE quantities, while the right column shows odd-order quantities. Comparisons between DBM simulations and analytical solutions with first- and second-order accuracy (see Table 2) are presented.

These TNE quantities offer insights into non-equilibrium characteristics from various perspectives:

(I) As the Mach number increases, the profiles of TNE quantities shift, with higher Mach numbers showing more pronounced deviations from equilibrium. At $Ma = 1.2$, the TNE quantities exhibit relatively small deviations. However, as the Mach number increases, the internal non-equilibrium states of the shock become more evident, particularly at the shock core.

(II) Even-order TNE quantities are positive, while odd-order TNE quantities are negative. The positive values of Δ_2^* [see Fig. 8(a)] indicate a positive deviation from equilibrium in momentum transfer, suggesting that momentum transport within the shock generally moves toward the compression region. Conversely, $\Delta_{3,1}^*$ shows that heat is transferred in the negative direction, while the heat conduction flux $\Delta_{4,2}^*$ is positive.

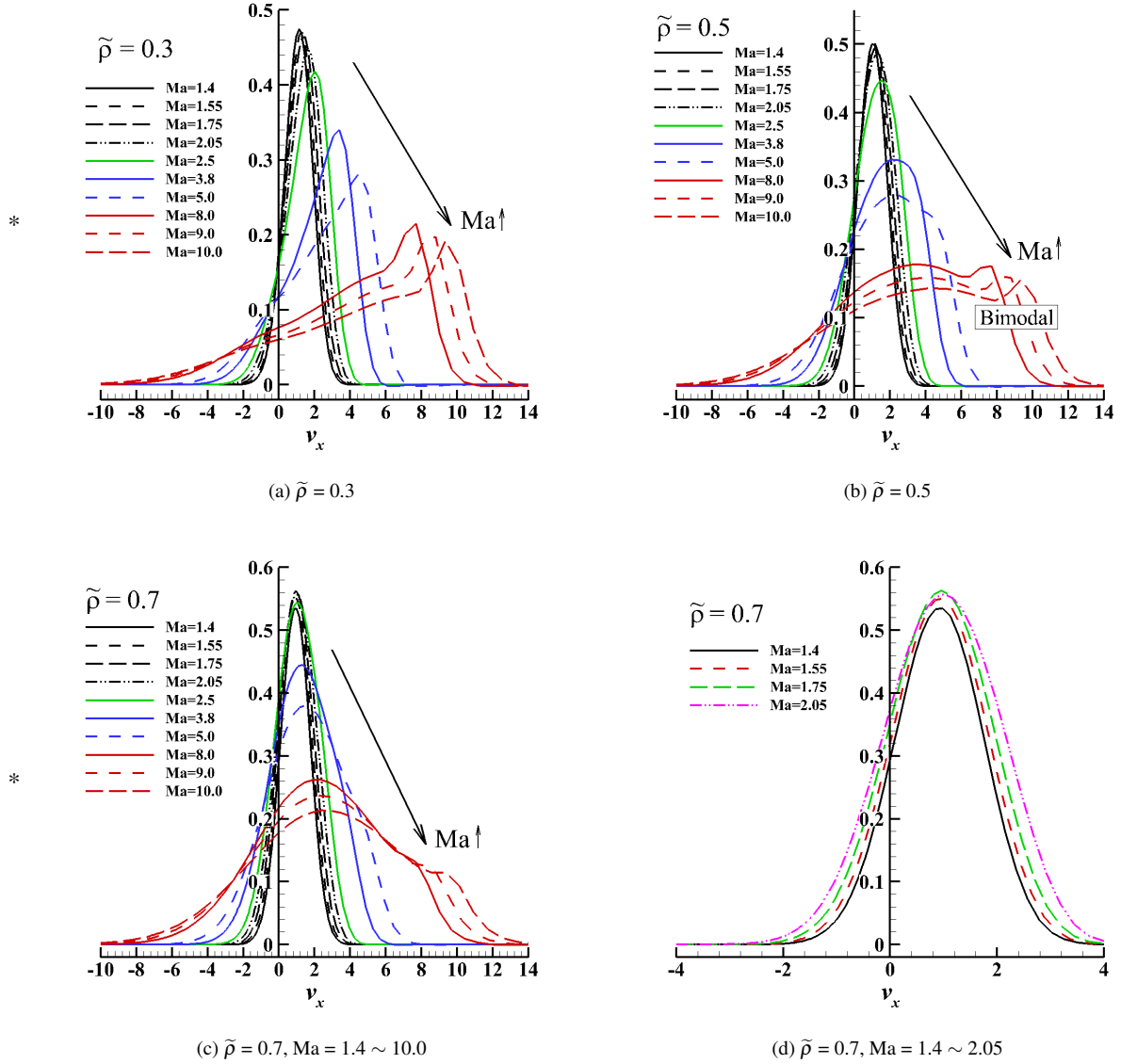


Figure 7: DBM simulations of the distribution functions g at positions with $\tilde{\rho} = 0.3, 0.5,$ and 0.7 , for Ma numbers ranging from 1.4 to 10.0

(III) For the same situation, as the order m of the TNE quantities increases, their magnitude significantly increases. For instance, Δ_4^* indicates a much higher TNE degree compared to that inferred from Δ_2^* .

By analyzing these quantities, especially through higher-order TNE effects, we can obtain a more detailed understanding of the shock structure and the dominant non-equilibrium mechanisms. The shift in distribution functions and their interaction across different Mach numbers underscores the importance of incorporating higher-order TNE effects for accurate shock modeling.

4.8.1. Non-equilibrium degree from perspective of TNE quantities

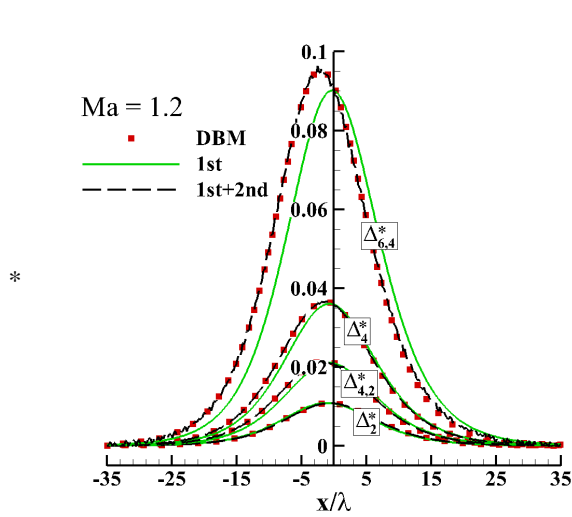
The non-equilibrium order considered in physical modeling depends on two factors: the order of relevant TNE quantities

and the required precision. The higher the order of the TNE quantities or the required precision, the higher the TNE order the model must consider. For example, as shown in Fig. 8(a), if only the Δ_2^* quantity is of interest, a first-order non-equilibrium model suffices. However, if higher-order TNE quantities are involved, a second-order model is necessary. Therefore, it is important to compare the TNE quantities of different orders between DBM simulations and analytical solutions. Such comparisons are essential for selecting the appropriate model order for fluid simulations.

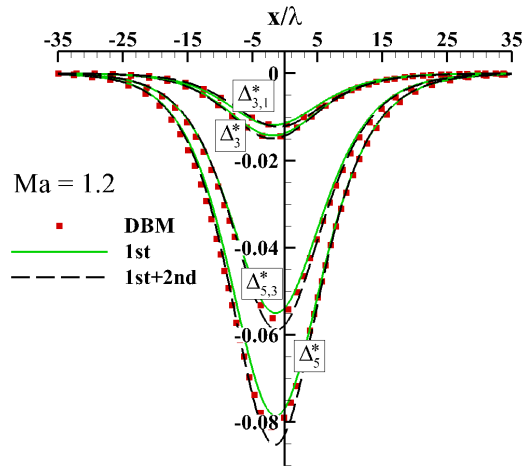
For $Ma = 1.2$ [see Figs. 8(a) and (b)], the following observations are made:

(I) The DBM simulation results closely align with the analytical solutions for both even- and odd-order TNE quantities.

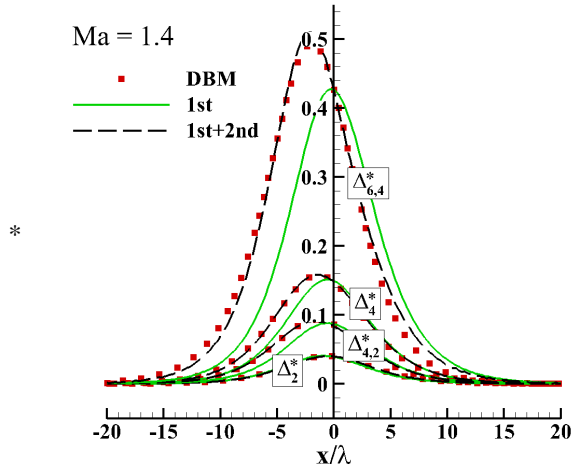
(II) Compared to the odd-order TNE quantities, the even-order ones show better agreement with the analytical solutions.



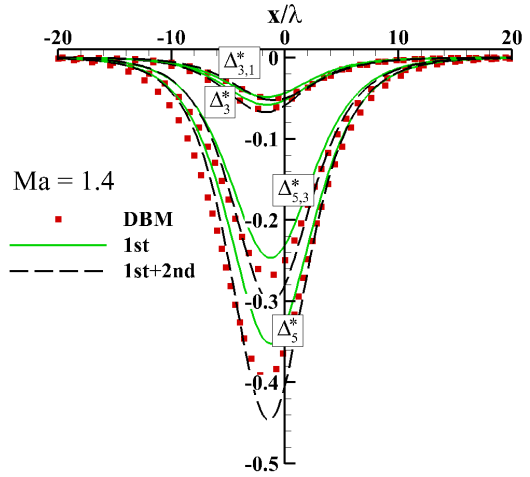
(a) Ma = 1.2, even-order: Δ_2^* , Δ_4^* , $\Delta_{4,2}^*$, and $\Delta_{6,4}^*$.



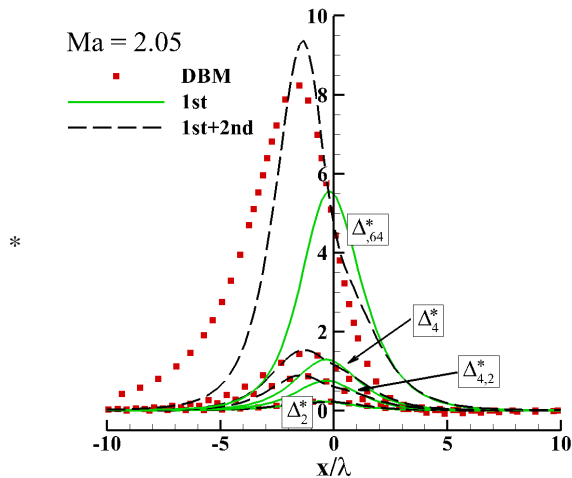
(b) Ma = 1.2, odd-order: Δ_3^* , Δ_5^* , $\Delta_{3,1}^*$, and $\Delta_{5,3}^*$.



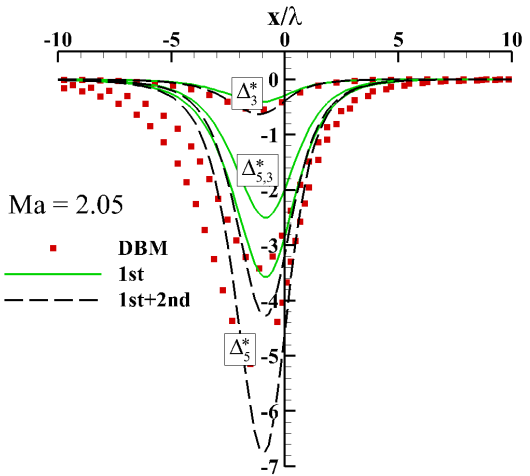
(c) Ma = 1.4, even-order: Δ_2^* , Δ_4^* , $\Delta_{4,2}^*$, and $\Delta_{6,4}^*$.



(d) Ma = 1.4, odd-order: Δ_3^* , Δ_5^* , $\Delta_{3,1}^*$, and $\Delta_{5,3}^*$.



(e) Ma = 2.05, even-order: Δ_2^* , Δ_4^* , $\Delta_{4,2}^*$, and $\Delta_{6,4}^*$.



(f) Ma = 2.05, odd-order: Δ_3^* , Δ_5^* , $\Delta_{3,1}^*$, and $\Delta_{5,3}^*$.

Figure 8: Comparisons of various TNE quantities between DBM simulation and analytical solutions for Ma numbers 1.2, 1.4, and 2.05, respectively. Here, “1st” refers to $\Delta_m^{*(1)}$ ($\Delta_{m,n}^{*(1)}$), “1st+2nd” refers to $\Delta_m^{*(1)} + \Delta_m^{*(2)}$ ($\Delta_{m,n}^{*(1)} + \Delta_{m,n}^{*(2)}$).

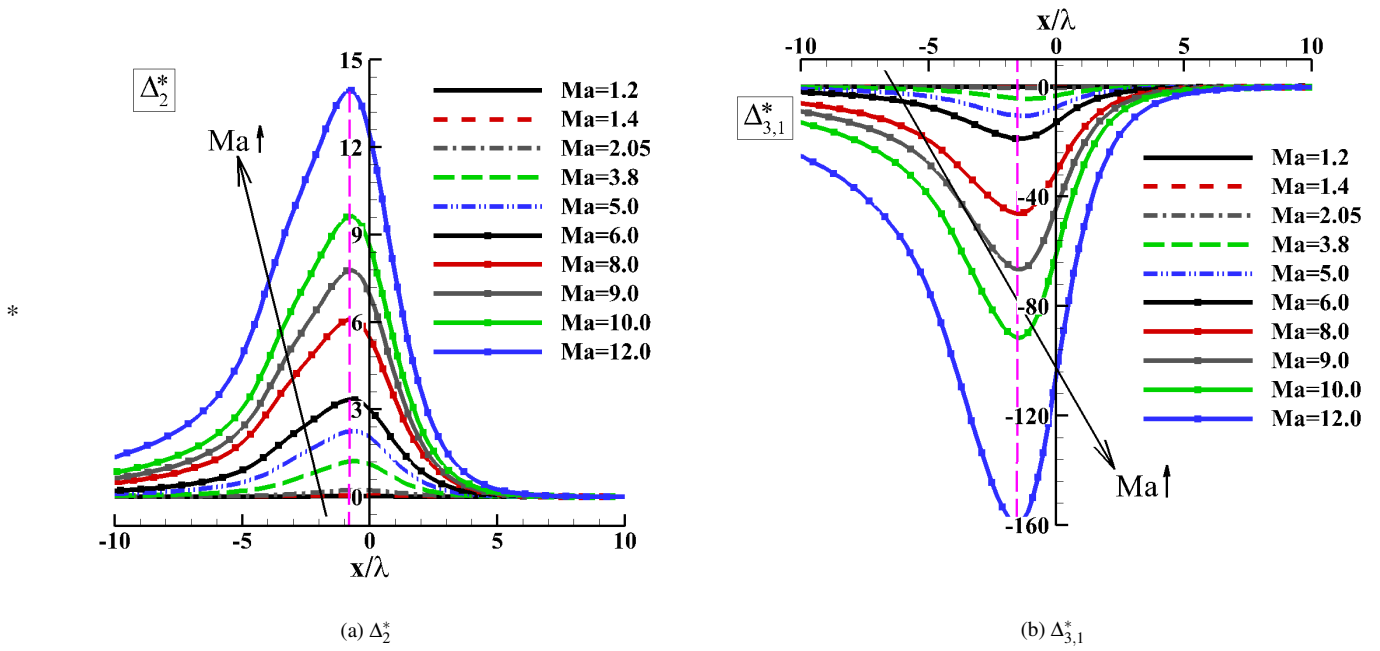


Figure 9: DBM simulations of Δ_2^* and $\Delta_{3,1}^*$ for Ma numbers ranging from 1.2 to 12.0.

This improved agreement is attributed to the stronger isotropy of even-order TNE quantities.

(III) As the order of TNE quantities increases, the differences between the first-order analytical and DBM simulation results also grow. Second-order (1st+2nd) analytical results show better alignment with DBM simulations compared to first-order (1st) solutions, reflecting their higher physical accuracy. For example, the second-order analytical solution for $\Delta_{6,4}^*$, as listed in Table 2, provides improved precision by incorporating second-order effects, including the reciprocal of density, velocity, and temperature profiles, rather than relying solely on first-order velocity effects.

(IV) As the TNE order increases, the peak location of TNE quantities shifts closer to the inflow region. This spatial shift highlights the differences in non-equilibrium descriptions captured by TNE quantities of varying orders.

For $Ma = 1.4$ [see Figs. 8(c) and (d)], the values of TNE quantities increase compared to $Ma = 1.2$, indicating a greater deviation from equilibrium. It is observed that:

(I) As the TNE degree intensifies, the first-order analytical solution shows significant deviations from the DBM simulation results. However, the second-order analytical solution maintains satisfactory agreement with the DBM simulations.

(II) As the order of TNE quantities increases, the discrepancies between the second-order analytical results and DBM simulations become more pronounced.

When the Mach number increases to 2.05, the TNE degree of the fluid further intensifies, resulting in even more significant differences between the second-order analytical results and DBM simulations. For lower-order TNE quantities, the second-order analytical results maintain their physical accuracies, while they lose accuracies for higher-order TNE quantities.

For convenience, some analysis results from various perspectives are listed in Table 4. It is clear that when analyzing TNE from different angles, the results may vary. This emphasizes the importance of describing non-equilibrium from multiple perspectives.

4.8.2. Effects of Mach numbers on TNE measures

To further examine the effects of Mach number on NOMF and NOEF inside shocks, Figs. 9(a) and (b) present the profiles of Δ_2^* and $\Delta_{3,1}^*$, respectively, for Mach numbers ranging from 1.2 to 12.0. Both Δ_2^* and $\Delta_{3,1}^*$ increase as the Mach number rises, indicating an intensification of non-equilibrium effects. From another perspective, it can also explain as that momentum transport and heat conduction over the x -direction intensify as the Mach number increases.

In Fig. 9(a), as the Mach number increases, the non-equilibrium region expands, with the peak of Δ_2^* shifting progressively closer to the inflow region. It is seen that effects of Mach numbers are not two-stage. The increase in Mach number results in a broader shock front and a thicker transition region, as reflected in the widening of the non-equilibrium region. In Fig. 9(b), the peak of $\Delta_{3,1}^*$ consistently shifts closer to the outflow region compared to Δ_2^* , with the gap between the two profiles widening at higher Mach numbers. This shift highlights the differing dynamics of momentum and heat transport in the shock.

Furthermore, as the Mach number increases, the peaks of both Δ_2^* and $\Delta_{3,1}^*$ shift progressively towards the inflow region. This trend indicates that, as the Mach number increases, the non-equilibrium effects are more pronounced in the shock's front region, emphasizing the increased influence of high-speed flow on the shock's internal structure.

Mach number	Perspective	Required TNE order
Ma = 1.2	$g - g^{(0)}$	First order
	Δ_2^*	First order
	$\Delta_{3,1}^*$	Second order
	Δ_3^*	Second order
	Higher-order even-order TNE quantities	Second order
	Higher-order odd-order TNE quantities	Beyond second order
Ma = 1.4	$g - g^{(0)}$	First order
	Δ_2^*	First order
	$\Delta_{3,1}^*$	Second order
	Δ_3^*	Second order
	Higher-order even-order TNE quantities	Second order
	Higher-order odd-order TNE quantities	Beyond second order
Ma = 1.55	$g - g^{(0)}$	First order
Ma = 1.75	$g - g^{(0)}$	Second order
Ma = 2.05	$g - g^{(0)}$	Second order
	Δ_2^*	First order
	Δ_3^*	Second order
	$\Delta_{4,2}^*$ and Δ_4^*	Second order
	$\Delta_{6,4}^*$	Beyond second order
	Higher-order odd-order TNE quantities	Beyond second order
Ma = 2.5	$g - g^{(0)}$	Second order
Ma = 3.8	$g - g^{(0)}$	Beyond third order

Table 4: TNE order required for different Mach numbers under various nonequilibrium perspectives in physical modeling.

5. Conclusion

Shock waves, as representative non-equilibrium flow phenomena, exhibit pronounced hydrodynamic nonequilibrium (HNE) and thermodynamic nonequilibrium (TNE) effects due to their inherently small-scale structures and rapid kinetic modes. Despite their ubiquity in natural and engineering systems, the underlying mechanisms driving HNE and TNE effects within shock structures remain insufficiently understood.

This study examines HNE and TNE characteristics in argon shock structures using a higher-order discrete Boltzmann method (DBM), a kinetic modeling framework for simulating discrete/ non-equilibrium effects and analyzing complex physical phenomena. A key feature of the DBM in this study is its direct discretization of velocity space, which preserves high-order HNE and TNE effects. To extract non-equilibrium manifestations, HNE and TNE quantities of different orders are defined using the non-conserved kinetic moments of $(f - f^{eq})$. To hierarchically investigate non-equilibrium mechanisms, higher-order analytical solutions for both distribution functions and TNE quantities are derived using Chapman-Enskog multiscale analysis, though DBM simulations do not depend on these theoretical results.

First, the accuracy of the multiscale DBM is validated by comparing macroscopic characteristics, such as interface profiles and thickness, from DBM simulations with experimental data and DSMC results. Next, the agreement between DBM simulations and analytical solutions is assessed at the mesoscopic level by comparing kinetic quantities such as distribution functions and TNE measures. Results indicate that analytical solutions incorporating higher-order TNE effects align more closely with DBM simulations than those restricted to lower-order effects.

The impact of Mach number on HNE characteristics is analyzed by examining the shape and thickness of density, temperature, and velocity interfaces. Key findings include: (i) The influence of Mach number on macroscopic quantities follows a two-stage trend, affecting both interface smoothness and thickness. (ii) As the Mach number increases, the region of strong compressibility shifts from the outflow vicinity to the inflow region. The effect of Mach number on TNE characteristics is further investigated through different TNE measures. The deviation patterns and amplitudes of these measures at different shock positions are analyzed from multiple perspectives. Results show that a higher Mach number significantly intensifies TNE and enlarges the non-equilibrium region.

As a hallmark of multiscale system complexity, non-equilibrium effects manifest differently across analytical perspectives. Understanding HNE and TNE characteristics in shock waves is crucial for multiscale model selection and provides kinetic insights into cross-scale coupling mechanisms governing complex macroscopic and mesoscopic phenomena. Future research will focus on developing high-order DBM models in two and three dimensions to explore richer and more intricate mesoscopic HNE and TNE characteristics, mechanisms, and governing principles. These studies will incorporate increased degrees of freedom, diverse non-equilibrium driving

forces, and enhanced spatiotemporal multiscale coupling.

Declaration of competing interest

The authors declare that they have no known competing financial interests or personal relationships that could have appeared to influence the work reported in this paper.

Acknowledgments

The authors would like to thank Prof. Yudong Zhang and Dr. Jiahui Song for their insightful discussions. We also acknowledge support from the National Natural Science Foundation of China (Grant Nos. 11875001 and 12172061), the Foundation of the National Key Laboratory of Computational Physics (Grant No. SYSQN2024-10), the High-level Talents Research Start-up Grant from Guangxi University (Grant No. ZX01080031224009), the Hebei Outstanding Youth Science Foundation (Grant No. A2023409003), the Central Guidance on Local Science and Technology Development Fund of Hebei Province (Grant No. 226Z7601G), the Opening Project of State Key Laboratory of Explosion Science and Safety Protection (Beijing Institute of Technology) (Grant No. KFJJ25-02M), and the Foundation of the National Key Laboratory of Shock Wave and Detonation Physics (Grant No. JCKYS2023212003).

References

- [1] U. Hwang, K. A. Flanagan, R. Petre, Chandra X-ray observation of a Mature Cloud-Shock Interaction in the Bright Eastern Knot Region of Puppis A, *Astrophysical Journal* 635 (1) (2005) 355–364.
- [2] Y. X. Liu, Z. Chen, L. F. Wang, Z. Y. Li, J. F. Wu, W. H. Ye, Y. J. Li, Dynamic of shock–bubble interactions and nonlinear evolution of ablative hydrodynamic instabilities initiated by capsule interior isolated defects, *Physics of Plasmas* 30 (4) (2023) 042302.
- [3] D. Gaitonde, Progress in Shock Wave/Boundary Layer Interactions, in: *Progress in Shock Wave/Boundary Layer Interactions*, Vol. 72, 2013. doi:10.2514/6.2013-2607.
- [4] J. E. Lingeman, J. A. McAteer, E. Gnessin, A. P. Evan, Shock wave lithotripsy: advances in technology and technique, *Nature Reviews Urology* 6 (2009) 660–670.
- [5] D. V. Gaitonde, M. C. Adler, Dynamics of Three-Dimensional Shock-Wave/Boundary-Layer Interactions, *Annual Review of Fluid Mechanics* 55 (Volume 55, 2023) (2023) 291–321.
- [6] H. Jiang, J. Liu, X. K. Che, Y. Du, W. Huang, F. Ding, T. T. Zhang, Magnetic field control of high-enthalpy shock wave/boundary-layer interactions using a fully implicit thermochemical non-equilibrium solver, *Aerospace Science and Technology* 141 (2023) 108507.
- [7] Y. Bao, R. F. Qiu, K. Zhou, T. Zhou, Y. X. Weng, K. Lin, Y. C. You, Study of shock wave/boundary layer interaction from the perspective of nonequilibrium effects, *Physics of Fluids* 34 (2022) 046109.
- [8] D. Ranjan, J. Oakley, R. Bonazza, Shock-bubble interactions, *Annual Review of Fluid Mechanics* 43 (2011) 117–140.
- [9] B. Zhang, H. Chen, B. Yu, M. S. He, H. Liu, Molecular simulation on viscous effects for microscale combustion in reactive shock–bubble interaction, *Combustion and flame* 208 (2019) 351–363.
- [10] X. Guo, Z. Y. Cong, T. Si, X. S. Luo, On Richtmyer–Meshkov finger collisions in a light fluid layer under reshock conditions, *Journal of Fluid Mechanics* 1000 (2024) A87.
- [11] J. C. Ding, D. Zhang, X. S. Luo, Divergent Richtmyer–Meshkov instability under different shock strengths, *Journal of Fluid Mechanics* 987 (2024) R5.

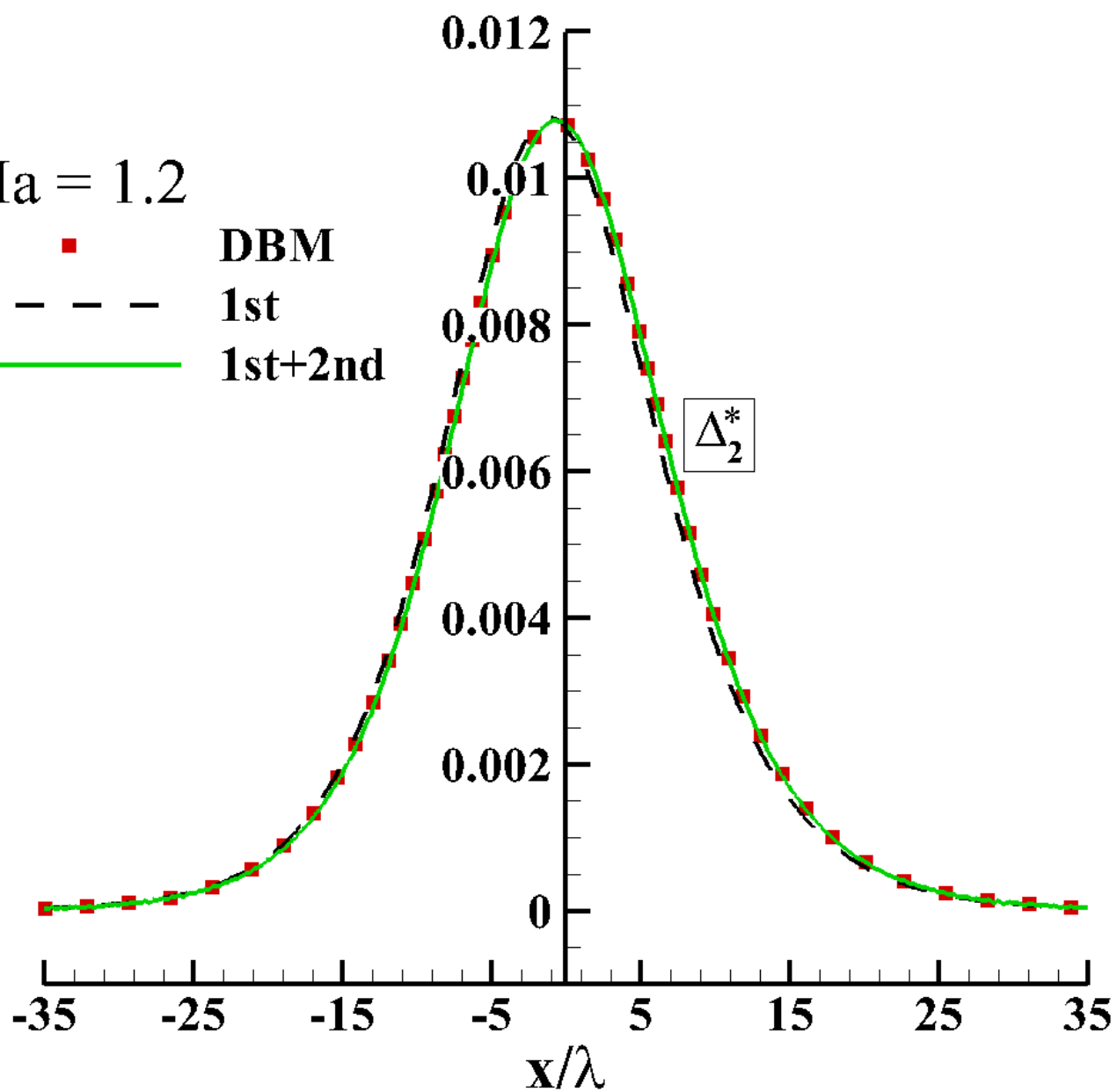
- [12] Z. G. Zhai, J. R. Xu, X. S. Luo, Convergent Richtmyer-Meshkov instability on two-dimensional tri-mode interfaces, *Science China-Physics Mechanics & Astronomy* 67 (2024) 124711.
- [13] H. B. Cai, W. S. Zhang, B. Du, X. X. Yan, L. Q. Shan, L. Hao, Z. C. Li, F. Zhang, T. Gong, D. Yang, S. Y. Zou, S. P. Zhu, X. T. He, Characteristic and impact of kinetic effects at interfaces of inertial confinement fusion hohlraums (in chinese), *High Power Laser and Particle Beams* 32 (09) (2020) 97–107.
- [14] R. F. Qiu, T. Zhou, Y. Bao, K. Zhou, H. H. Che, Y. C. You, Mesoscopic kinetic approach for studying nonequilibrium hydrodynamic and thermodynamic effects of shock wave, contact discontinuity, and rarefaction wave in the unsteady shock tube, *Physical Review E* 103 (2021) 053113.
- [15] J. Y. Yang, S. H. Zeng, Z. W. Wen, Z. Z. Jiang, C. W. Fang, Y. L. Qiu, Numerical assessment of double lateral jets interaction in rarefied nonequilibrium crossflows via nonlinear coupled constitutive relations, *Aerospace Science and Technology* 157 (2025) 109851.
- [16] J. C. Zhang, Z. G. Wang, C. Y. Liu, M. B. Sun, H. B. Wang, J. D. Ai, Z. H. Zhang, Thermo-chemical nonequilibrium effects on combustion characteristics of a transverse jet in the scramjet, *Aerospace Science and Technology* 152 (2024) 109357.
- [17] W. Q. Zhang, X. W. Wang, Z. J. Zhang, F. Han, S. S. Zhao, Heat and drag reduction of single and combined opposing jets in hypersonic nonequilibrium flows, *Aerospace Science and Technology* 121 (2022) 107194.
- [18] J. C. Zhang, C. S. Nie, J. S. Cai, S. C. Pan, An implicit coupling framework for numerical simulations between hypersonic nonequilibrium flows and thermal responses of charring materials in the presence of ablation, *Aerospace Science and Technology* 158 (2025) 109915.
- [19] H. Jin, W. C. Lin, F. Hu, X. Wu, Z. C. Sui, Y. C. You, Quantum-classical thermodynamic heterogeneous surface catalysis model in dilute non-equilibrium hypersonic flows, *Aerospace Science and Technology* 158 (2025) 109916.
- [20] S. Q. Guo, W. Liu, C. A. Zhang, Y. Liu, F. M. Wang, Aerodynamic optimization of hypersonic blunted waveriders based on symbolic regression, *Aerospace Science and Technology* 144 (2024) 108801.
- [21] K. C. K. Uy, J. A. Hao, R. Zhao, C.-Y. Wen, Stabilization of hypersonic boundary-layer instability using porous coatings under thermochemical nonequilibrium, *Aerospace Science and Technology* 141 (2023) 108520.
- [22] Y. G. Gao, Y. Liu, D. Ma, Effect of operation pressure on heat release characteristics in solid rocket motor nozzle considering detailed chemical reaction mechanism, *Aerospace Science and Technology* 128 (2022) 107794.
- [23] J. H. Guo, G. P. Lin, J. Zhang, X. Bu, H. Li, Hypersonic aerodynamics of a deformed aeroshell in continuum and near-continuum regimes, *Aerospace Science and Technology* 93 (2019) 105296.
- [24] H. M. Mott-Smith, The Solution of the Boltzmann Equation for a Shock Wave, *Physical Review* 82 (1951) 885–892.
- [25] G. A. Bird, *Molecular gas dynamics*, Oxford: Clarendon Press, 1976.
- [26] H. Alsmeyer, Density profiles in argon and nitrogen shock waves measured by the absorption of an electron beam, *Journal of Fluid Mechanics* 74 (1976) 497–513.
- [27] G. Pham-Van-Diep, D. Erwin, E. Muntz, Nonequilibrium Molecular Motion in a Hypersonic Shock Wave, *Science* 245 (1989) 624–626.
- [28] D. Gilbarg, D. Paolucci, The Structure of Shock Waves in the Continuum Theory of Fluids, *Journal of Rational Mechanics and Analysis* 2 (1953) 617–642.
- [29] J. D. Foch, On Higher Order Hydrodynamic Theories of Shock Structure, in: E. G. D. Cohen, W. Thirring (Eds.), *The Boltzmann Equation*, Springer Vienna, Vienna, 1973, pp. 123–140.
- [30] D. Burnett, The distribution of molecular velocities and the mean motion in a non-uniform gas, *Proceedings of the London Mathematical Society* 2 (1) (1936) 382–435.
- [31] W. W. Zhao, W. F. Chen, R. K. Agarwal, Formulation of a new set of Simplified Conventional Burnett equations for computation of rarefied hypersonic flows, *Aerospace Science and Technology* 38 (2014) 64–75.
- [32] H. Grad, On the kinetic theory of rarefied gases, *Communications on Pure and Applied Mathematics* 2 (4) (1949) 331–407.
- [33] H. Struchtrup, M. Torrilhon, Regularization of Grad’s 13 moment equations: Derivation and linear analysis, *Physics of Fluids* 15 (9) (2003) 2668–2680.
- [34] M. Torrilhon, H. Struchtrup, Regularized 13-moment equations: shock structure calculations and comparison to Burnett models, *Journal of Fluid Mechanics* 513 (25) (2004) 171–198.
- [35] S. Succi, *The lattice boltzmann equation for fluid dynamics and beyond*, Oxford University Press, New York, 2001.
- [36] K. Hejranfar, A. Ghaffarian, A high-order accurate unstructured spectral difference lattice Boltzmann method for computing inviscid and viscous compressible flows, *Aerospace Science and Technology* 98 (2020) 105661.
- [37] Y. L. Feng, S. L. Guo, J. Jacob, P. Sagaut, Grid refinement in the three-dimensional hybrid recursive regularized lattice Boltzmann method for compressible aerodynamics, *Physical Review E* 101 (2020) 063302.
- [38] S. Zhao, G. Farag, P. Boivin, P. Sagaut, Toward fully conservative hybrid lattice Boltzmann methods for compressible flows, *Physics of Fluids* 32 (12) (2020) 126118.
- [39] H. Y. Huang, K. Jin, K. Li, H. Li, X. J. Zheng, An implicit lattice Boltzmann method for simulations of compressible plasma kinetics, *Physics of Fluids* 36 (8) (2024) 086128.
- [40] L. L. Fei, F. F. Qin, G. Wang, J. W. Huang, B. H. Wen, J. L. Zhao, K. H. Luo, D. Derome, J. Carmeliet, Coupled lattice Boltzmann method–discrete element method model for gas–liquid–solid interaction problems, *Journal of Fluid Mechanics* 975 (2023) A20.
- [41] Z. Chen, C. Shu, L. M. Yang, X. Zhao, N. Y. Liu, Phase-field-simplified lattice boltzmann method for modeling solid-liquid phase change, *Phys. Rev. E* 103 (2021) 023308.
- [42] S. Busuioic, V. Sofonea, Bounded flows of dense gases, *Phys. Rev. Fluids* 9 (2024) 023401.
- [43] K. Xu, J. C. Huang, A unified gas-kinetic scheme for continuum and rarefied flows, *Journal of Computational Physics* 229 (20) (2010) 7747–7764.
- [44] R. Zhang, S. Liu, J. F. Chen, H. Jin, C. S. Zhuo, C. W. Zhong, Implicit unified gas-kinetic scheme for steady state solution of hypersonic thermodynamic non-equilibrium flows, *Communications in Nonlinear Science and Numerical Simulation* 140 (2024) 108367.
- [45] Y. J. Zhu, C. W. Zhong, K. Xu, An implicit unified gas-kinetic scheme for unsteady flow in all Knudsen regimes, *Journal of Computational Physics* 386 (2019) 190–217.
- [46] Z. L. Guo, R. J. Wang, K. Xu, Discrete unified gas kinetic scheme for all Knudsen number flows. II. Thermal compressible case, *Physical Review E* 91 (2015) 033313.
- [47] C. Liu, Y. J. Zhu, K. Xu, Unified gas-kinetic wave-particle methods I: Continuum and rarefied gas flow, *Journal of Computational Physics* 401 (2020) 108977.
- [48] Y. F. Wei, Y. J. Zhu, K. Xu, Unified gas-kinetic wave-particle methods VII: Diatomic gas with rotational and vibrational nonequilibrium, *Journal of Computational Physics* 497 (2024) 112610.
- [49] S. Liu, K. Xu, C. W. Zhong, Progress of the unified wave-particle methods for non-equilibrium flows from continuum to rarefied regimes, *Acta Mechanica Sinica* 38 (2022) 122123.
- [50] Q. Li, J. Zeng, L. Wu, Kinetic modelling of rarefied gas mixtures with disparate mass in strong non-equilibrium flows, *Journal of Fluid Mechanics* 1001 (2024) A5.
- [51] Z. Y. Yuan, W. W. Zhao, Z. Z. Jiang, W. F. Chen, Numerical simulation of hypersonic reaction flows with nonlinear coupled constitutive relations, *Aerospace Science and Technology* 112 (2021) 106591.
- [52] Z. H. Li, H. X. Zhang, Gas-kinetic description of shock wave structures by solving Boltzmann model equation, *International Journal of Computational Fluid Dynamics* 22 (2008) 623–638.
- [53] Z. H. Li, A. P. Peng, H. X. Zhang, J. Y. Yang, Rarefied gas flow simulations using high-order gas-kinetic unified algorithms for Boltzmann model equations, *Progress in Aerospace Sciences* 74 (2015) 81–113.
- [54] N. G. Kallikounis, B. Dorschner, I. V. Karlin, Particles on demand for flows with strong discontinuities, *Physical Review E* 106 (2022) 015301.
- [55] Y. Ji, S. A. Hosseini, B. Dorschner, K. Luo, I. Karlin, Eulerian discrete kinetic framework in comoving reference frame for hypersonic flows, *Journal of Fluid Mechanics* 983 (2024) A11.
- [56] L. M. Yang, C. Shu, J. Wu, Y. Y. Liu, X. Shen, An efficient discrete velocity method with inner iteration for steady flows in all flow regimes, *Physics of Fluids* 34 (2) (2022) 027110.
- [57] A. G. Xu, D. J. Zhang, Y. B. Gan, Advances in the kinetics of heat and mass transfer in near-continuous complex flows, *Frontiers of Physics* 19 (2024) 425000.
- [58] A. Xu, Y. Zhang, *Complex Media Kinetics* (in Chinese), Beijing: Science

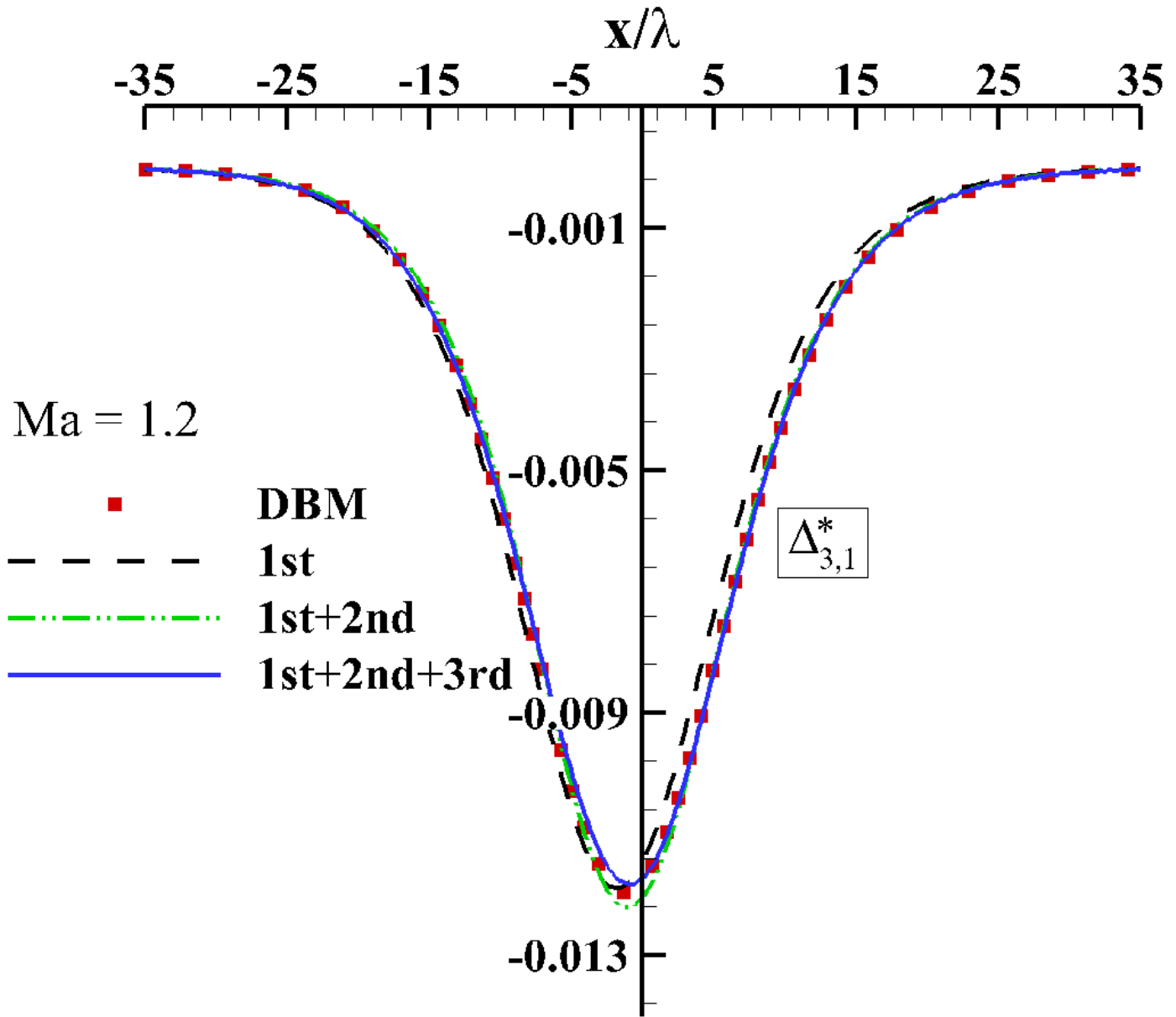
Press, 2022.

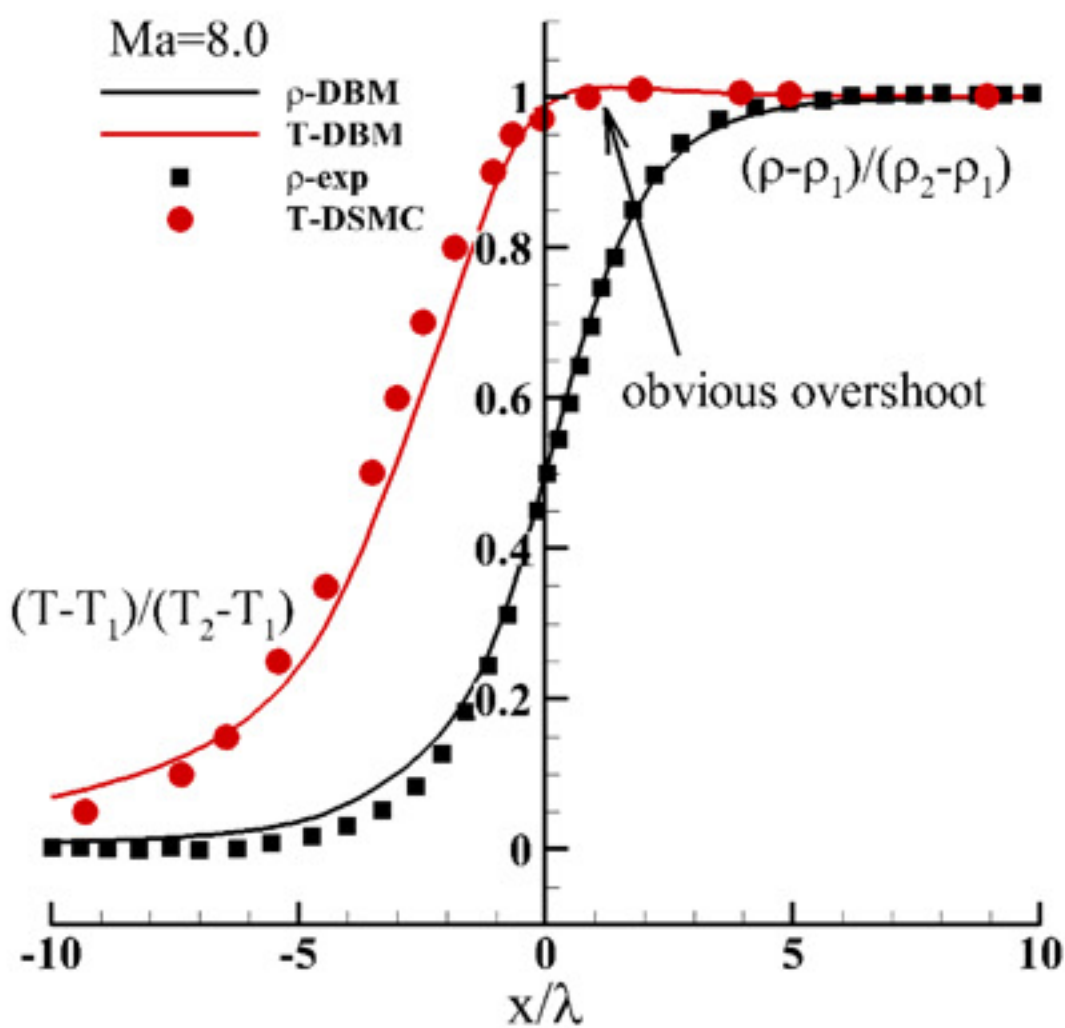
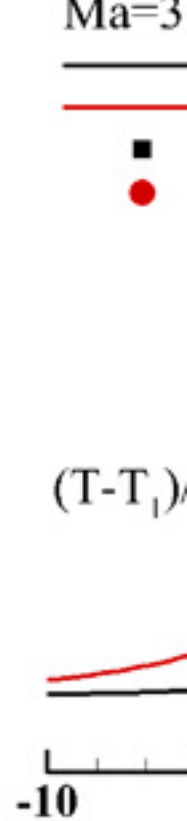
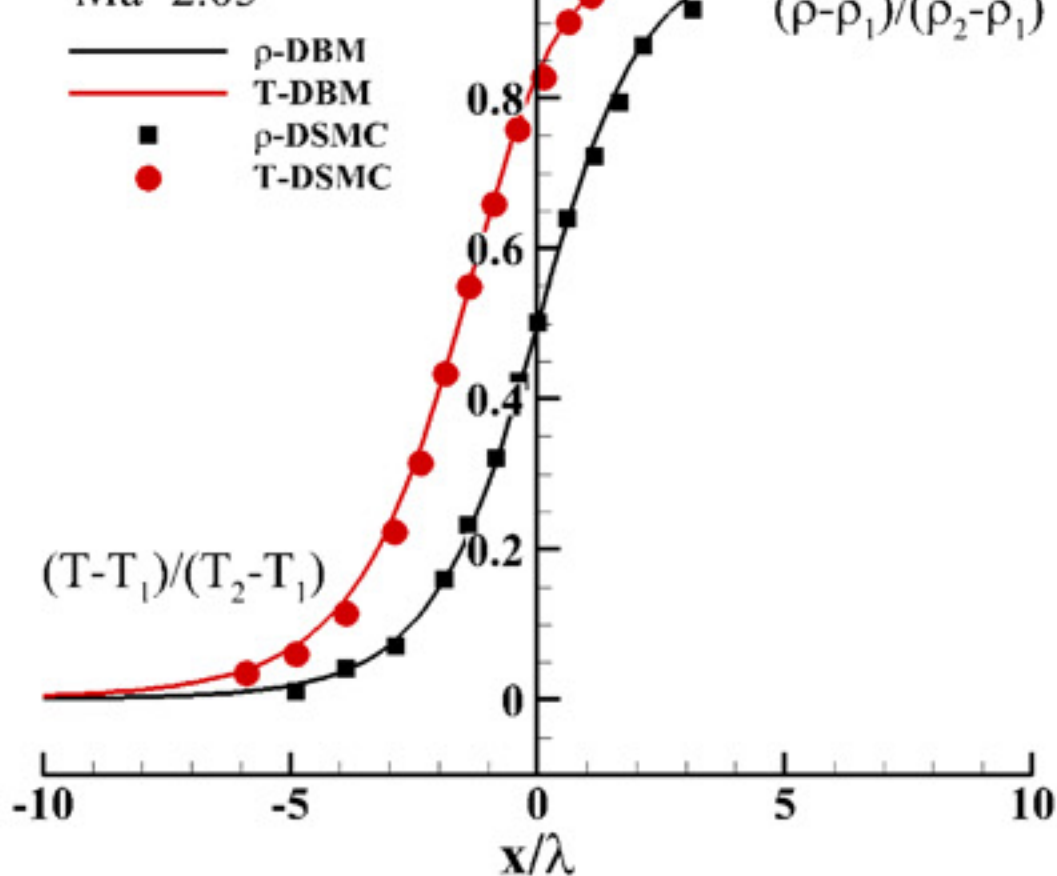
- [59] Y. Gan, A. G. Xu, G. Zhang, S. Succi, Discrete Boltzmann modeling of multiphase flows: hydrodynamic and thermodynamic non-equilibrium effects, *Soft Matter* 11 (26) (2015) 5336–5345.
- [60] Y. B. Gan, A. G. Xu, H. L. Lai, W. Li, G. L. Sun, S. Succi, Discrete Boltzmann multi-scale modelling of non-equilibrium multiphase flows, *Journal of Fluid Mechanics* 951 (2022) A8.
- [61] J. Chen, A. G. Xu, D. W. Chen, Y. D. Zhang, Z. H. Chen, Discrete Boltzmann modeling of Rayleigh–Taylor instability: effects of interfacial tension, viscosity and heat conductivity, *Physical Review E* 106 (2022) 015102.
- [62] Y. M. Shan, A. G. Xu, L. F. Wang, Y. D. Zhang, Nonequilibrium kinetics effects in Richtmyer–Meshkov instability and reshock processes, *Communications in Theoretical Physics* 75 (11) (2023) 115601.
- [63] H. L. Lai, A. G. Xu, G. C. Zhang, Y. B. Gan, Y. J. Ying, S. Succi, Nonequilibrium thermohydrodynamic effects on the Rayleigh–Taylor instability in compressible flows, *Physical Review E* 94 (2016) 023106.
- [64] Y. F. Li, C. D. Lin, Kinetic investigation of Kelvin–Helmholtz instability with nonequilibrium effects in a force field, *Physics of Fluids* 36 (2024) 116140.
- [65] J. Chen, A. G. Xu, Y. D. Zhang, D. W. Chen, Z. H. Chen, Kinetics of Rayleigh–Taylor instability in van der Waals fluid: the influence of compressibility, *Frontiers of Physics* 20 (1) (2025) 11201.
- [66] Y. D. Zhang, X. Wu, B. B. Nie, A. G. Xu, F. Chen, R. H. Wei, Lagrangian steady-state discrete Boltzmann model for non-equilibrium flows at micro–nanoscale, *Physics of Fluids* 35 (9) (2023) 092008.
- [67] C. D. Lin, K. H. Luo, Mesoscopic simulation of nonequilibrium detonation with discrete Boltzmann method, *Combustion and Flame* 198 (2018) 356–362.
- [68] J. H. Song, A. G. Xu, L. Miao, Plasma kinetics: Discrete Boltzmann modelling and Richtmyer–Meshkov instability, *Physics of Fluids* 36 (2024) 016107.
- [69] F. Chen, A. G. Xu, G. C. Zhang, Collaboration and Competition Between Richtmyer–Meshkov instability and Rayleigh–Taylor instability, *Physics of Fluids* 30 (10) (2018) 102105.
- [70] D. J. Zhang, A. G. Xu, Y. B. Gan, Y. D. Zhang, J. H. Song, Y. J. Li, Viscous effects on morphological and thermodynamic non-equilibrium characterizations of shock–bubble interaction, *Physics of Fluids* 35 (10) (2023) 106113.
- [71] Y. B. Gan, A. G. Xu, G. C. Zhang, Y. D. Zhang, S. Succi, Discrete Boltzmann trans-scale modeling of high-speed compressible flows, *Physical Review E* 97 (2018) 053312.
- [72] D. J. Zhang, A. G. Xu, Y. D. Zhang, Y. B. Gan, Y. J. Li, Discrete Boltzmann modeling of high-speed compressible flows with various depths of non-equilibrium, *Physics of Fluids* 34 (8) (2022) 086104.
- [73] A. G. Xu, G. C. Zhang, Y. B. Gan, F. Chen, X. J. Yu, Lattice Boltzmann modeling and simulation of compressible flows, *Frontiers of Physics* 7 (2012) 582–600.
- [74] Z. H. Li, H. X. Zhang, Gas-kinetic description of shock wave structures by solving Boltzmann model equation (in chinese), *ACTA Aerodynamica Sinica* 25 (04) (2007) 411–418+436.
- [75] Y. M. Shan, A. G. Xu, Y. D. Zhang, L. F. Wang, Wall-heating phenomena in shock wave physics: Physical or artificial? (in preparation) (2025).
- [76] Y. B. Gan, Z. W. Zhuang, B. Yang, A. G. Xu, D. J. Zhang, F. Chen, J. H. Song, Y. H. Wu, Supersonic flow kinetics: Mesoscale structures, thermodynamic nonequilibrium effects and entropy production mechanisms (in preparation) (2025).

Ma = 1.2

- DBM
- - - 1st
- 1st+2nd

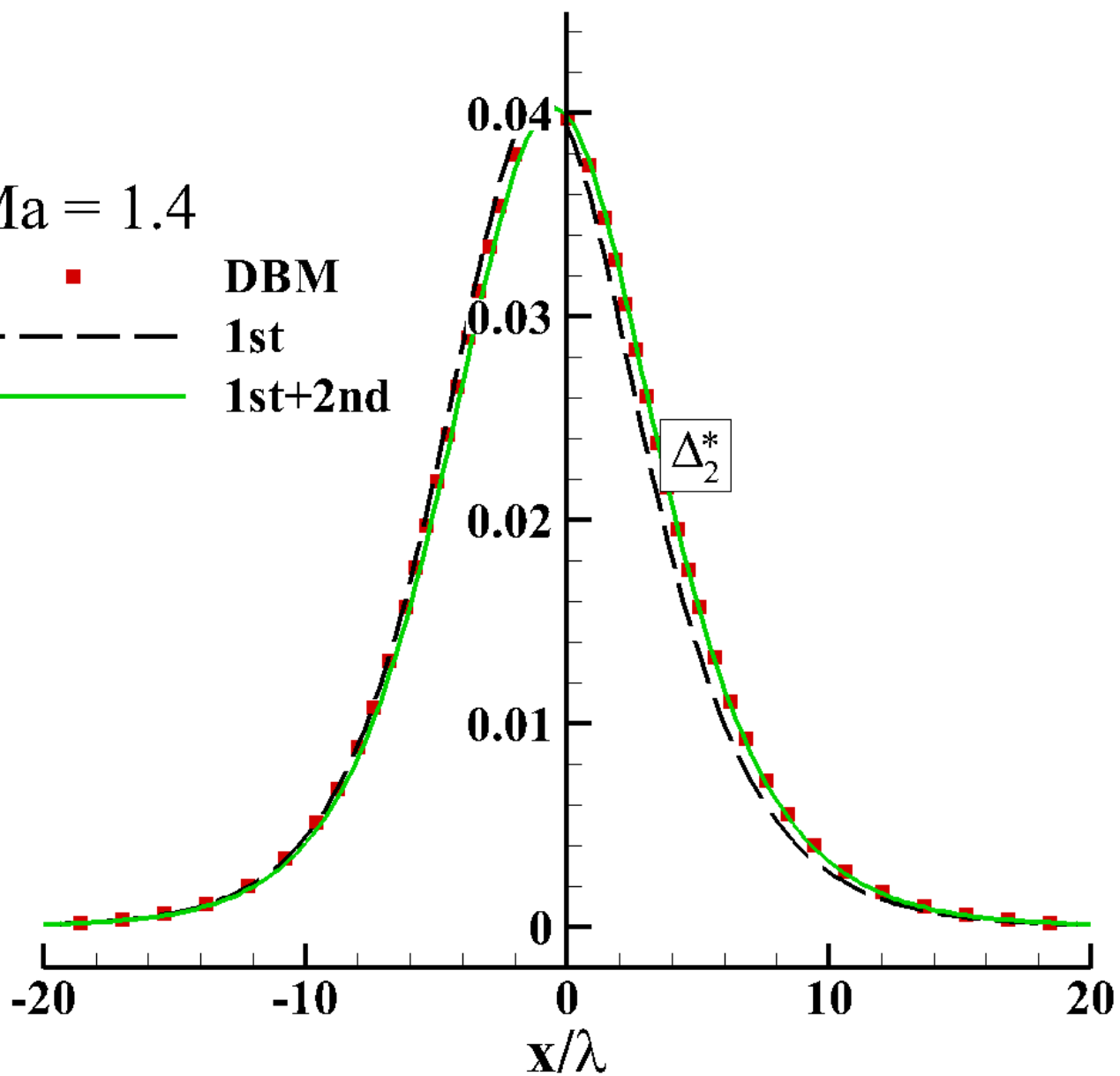


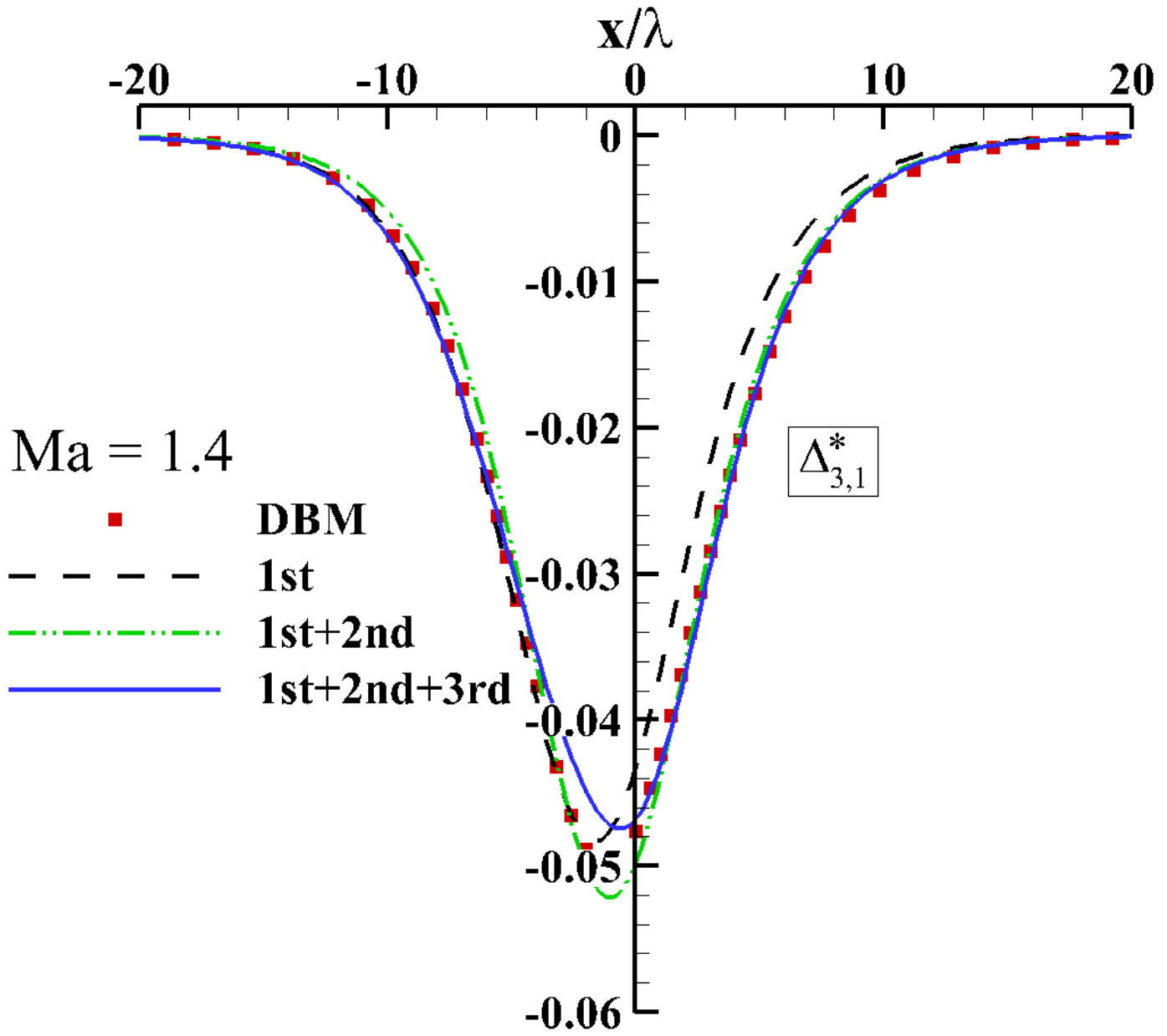




Ma = 1.4

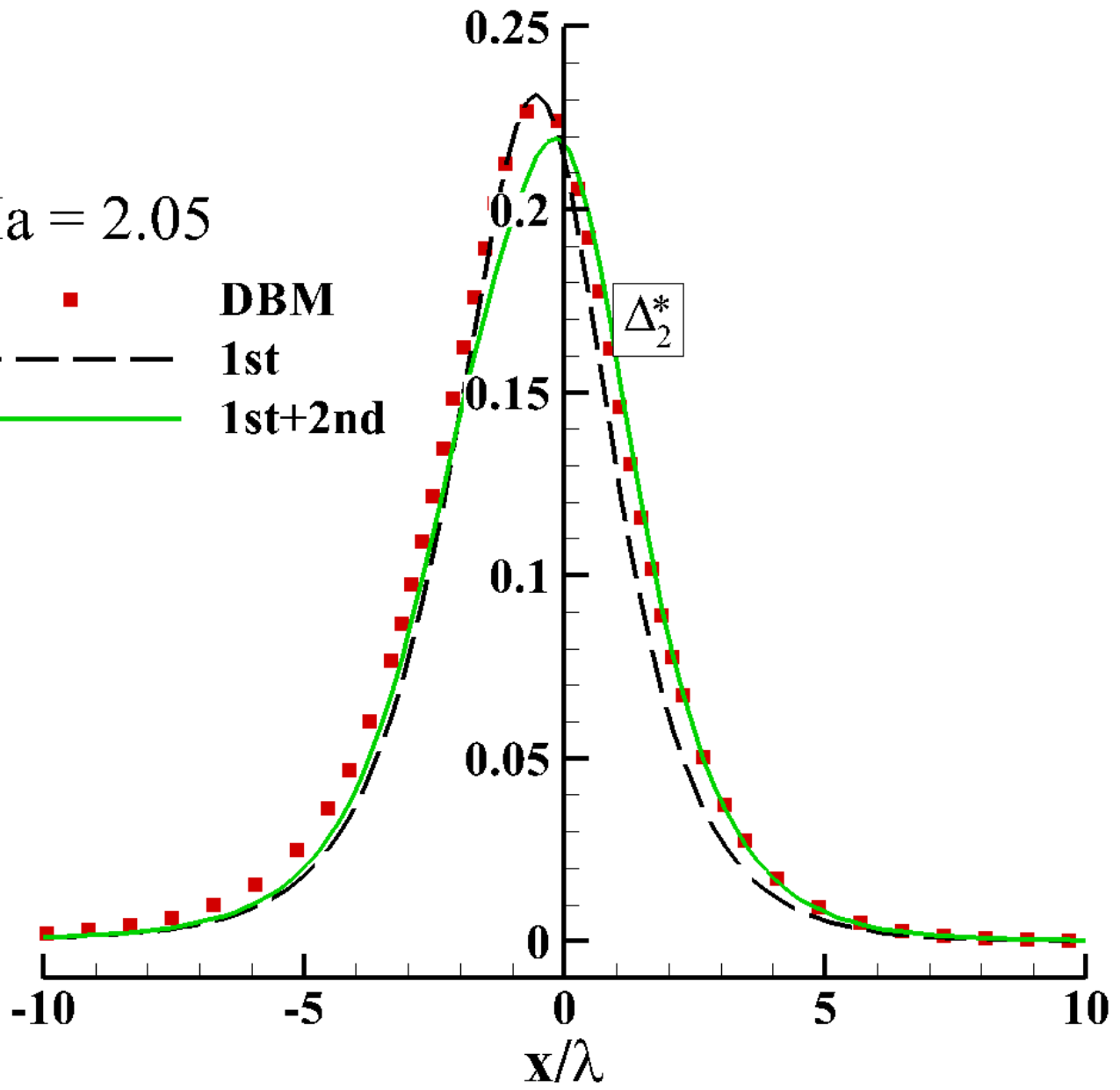
■ DBM
- - - 1st
— 1st+2nd

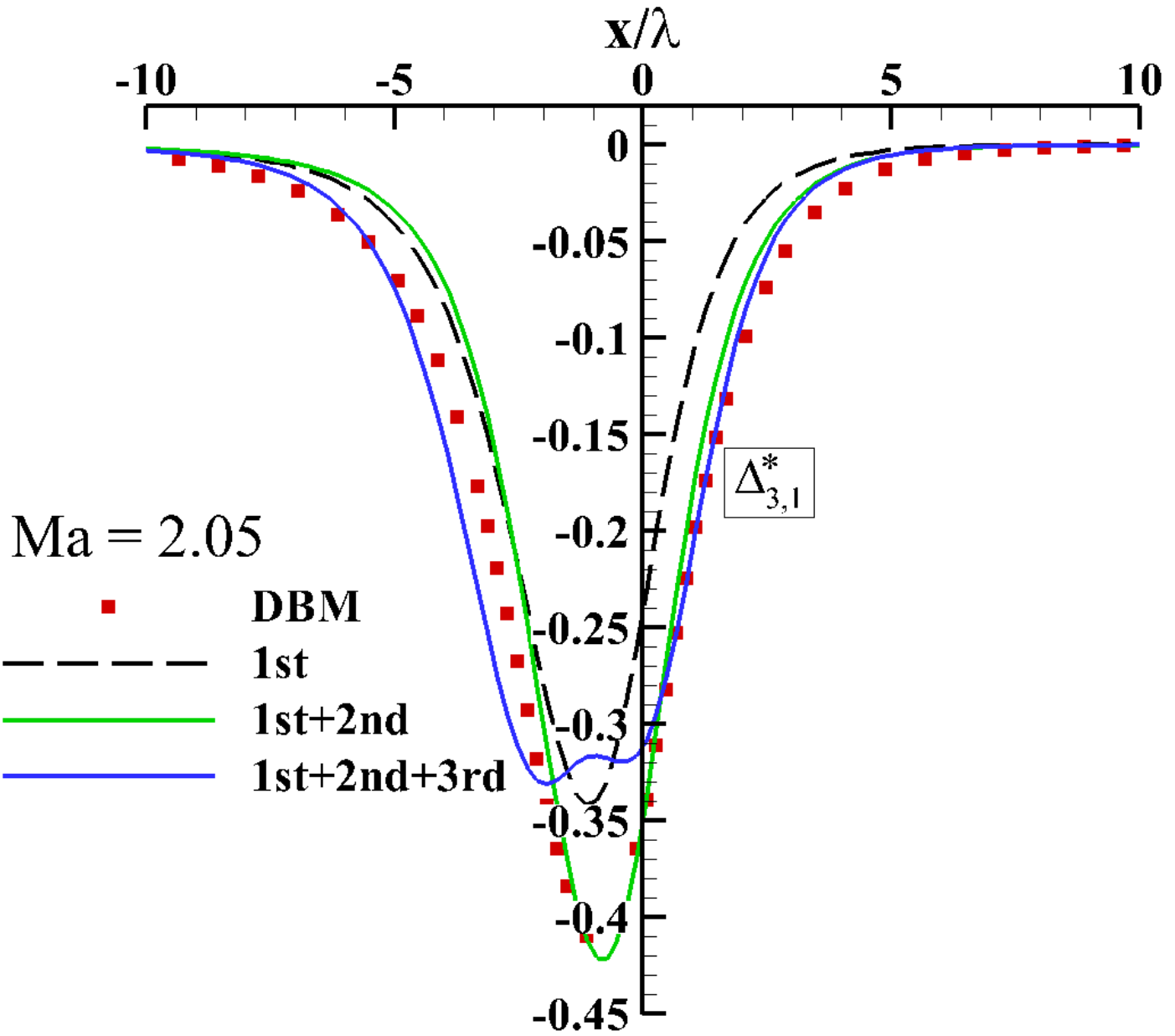




Ma = 2.05

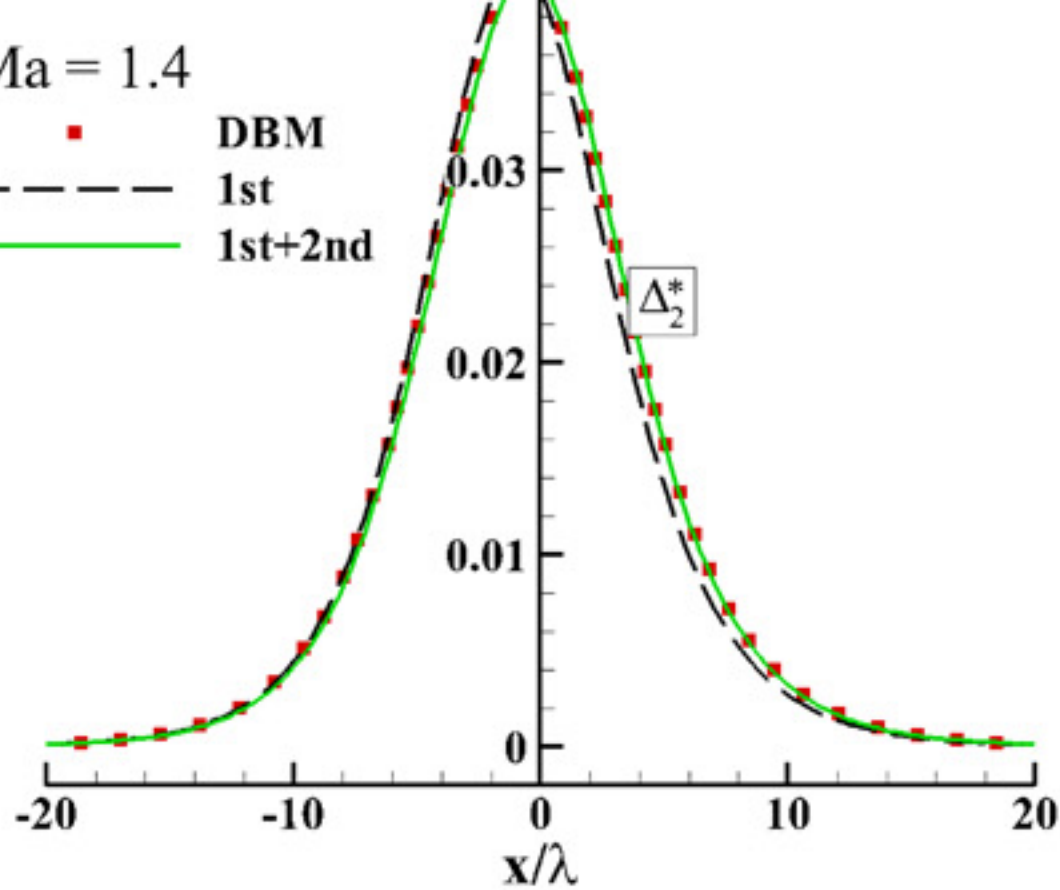
- DBM
- 1st
- 1st+2nd





Ma = 1.4

■ DBM
- - - 1st
— 1st+2nd



(e)

Ma = 2.05

■ DBM
- - - 1st
— 1st+2nd

